

AD-9191 336

TIP VORTICES OF ISOLATED WINGS AND HELICOPTER ROTOR

1/1

BLADES(U) JAI ASSOCIATES INC MOUNTAIN VIEW CA

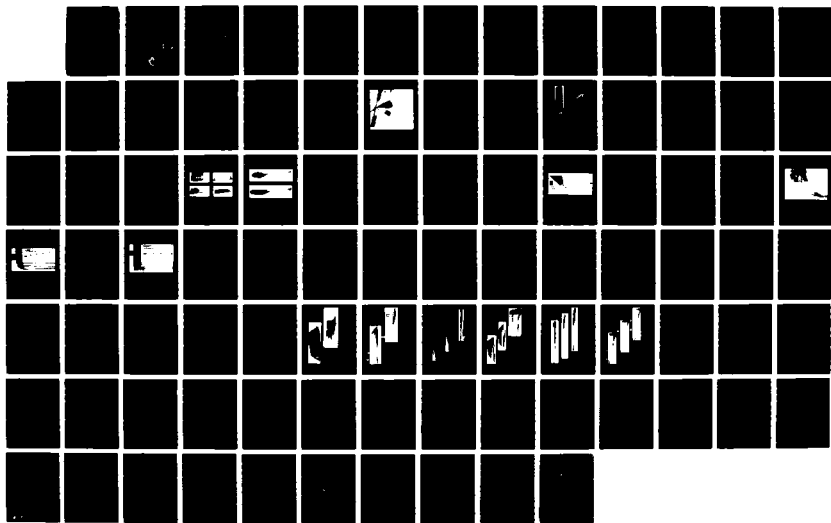
G R SRINIVASAN DEC 87 JAIA-TR-87-01 R/D-5378-PH-01

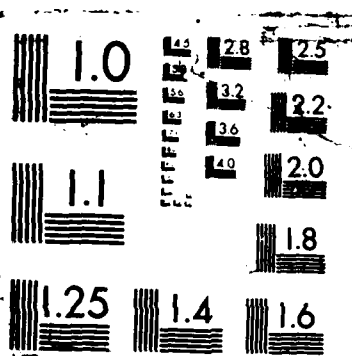
F/G 1/1

UNCLASSIFIED

DAAG29-85-C-0002

ML





AD-A191 336

217316-EG

(2)

DTIC FILE COPY

JAI Associates, Inc. Technical Report 87-01

**TIP VORTICES OF ISOLATED WINGS
AND HELICOPTER ROTOR BLADES**

by

Ganapathi R. Srinivasan

DTIC
ELECTED
FEB 04 1988
S H D



JAI ASSOCIATES
SCIENCE & ENGINEERING CONSULTANTS

DISTRIBUTION STATEMENT A

Approved for public release;
Distribution Unlimited

88 1 29 036

(2)

JAI Associates, Inc. Technical Report 87-01

**TIP VORTICES OF ISOLATED WINGS
AND HELICOPTER ROTOR BLADES**

by

Ganapathi R. Srinivasan

DTIC
SELECTED
FEB 04 1988
S D

H

ca

JAI Associates, Inc.
P. O. Box 293
Mountain View, California 94042

December 1987

Final Report of the Contract DAAG29-85-C-0002

November 1984 - November 1987



Prepared for

U. S. Army Research Office
P. O. Box 12211
Research Triangle Park, North Carolina 27709-2211

Accession For

NTIS GRA&I	<input checked="" type="checkbox"/>
DTIC TAB	<input type="checkbox"/>
Downgraded	<input type="checkbox"/>
Distribution	<input type="checkbox"/>
Availability	<input type="checkbox"/>
Serials	<input type="checkbox"/>
By	<input type="checkbox"/>
Distribution	<input type="checkbox"/>
Availability	<input type="checkbox"/>
Serials	<input type="checkbox"/>
Dist	<input type="checkbox"/>
Sp	<input type="checkbox"/>

A-1

DISTRIBUTION STATEMENT A

Approved for public release
Distribution Unlimited

UNCLASSIFIED

SECURITY CLASSIFICATION OF THIS PAGE (When Data Entered)

REPORT DOCUMENTATION PAGE		READ INSTRUCTIONS BEFORE COMPLETING FORM
1. REPORT NUMBER 21731.6-EL-5	2. GOVT ACCESSION NO. N/A	3. RECIPIENT'S CATALOG NUMBER N/A
4. TITLE (and Subtitle) TIP VORTICES OF ISOLATED WINGS AND HELICOPTER ROTOR BLADES		5. TYPE OF REPORT & PERIOD COVERED Final Report November 1984 - November 1987
		6. PERFORMING ORG. REPORT NUMBER JAIA TR-87-01
7. AUTHOR(s) Ganapathi R. Srinivasan		8. CONTRACT OR GRANT NUMBER(s) DAAG29-85-C-0002
9. PERFORMING ORGANIZATION NAME AND ADDRESS JAI Associates, Inc. P. O. Box 293 Mountain View, California 94042		10. PROGRAM ELEMENT, PROJECT, TASK AREA & WORK UNIT NUMBERS N/A
11. CONTROLLING OFFICE NAME AND ADDRESS U. S. Army Research Office Post Office Box 12211 Research Triangle Park, NC 27709		12. REPORT DATE December 1987
		13. NUMBER OF PAGES 82
14. MONITORING AGENCY NAME & ADDRESS (if different from Controlling Office)		15. SECURITY CLASS. (of this report) Unclassified
		15a. DECLASSIFICATION/DOWNGRADING SCHEDULE
16. DISTRIBUTION STATEMENT (of this Report) Approved for public release; distribution unlimited.		
17. DISTRIBUTION STATEMENT (of the abstract entered in Block 20, if different from Report) NA		
18. SUPPLEMENTARY NOTES The view, opinions, and/or findings contained in this report are those of the author(s) and should not be construed as an official Department of the Army position, policy, or decision, unless so designated by other documentation.		
19. KEY WORDS (Continue on reverse side if necessary and identify by block number) Viscous, unsteady flows; Zonal grid topology Thin layer Navier-Stokes; Tip Vortices Inertial reference frame; Three-dimensional flow separation steady flows and and		
20. ABSTRACT (Continue on reverse side if necessary and identify by block number) Thin layer Navier-Stokes equations are solved numerically for simulating the flowfields of isolated wings and helicopter rotor blades with a particular emphasis on understanding the formation and roll-up of tip vortices in subsonic and transonic flows. Several test cases consisting of wings and rotor blades of different planforms have been considered to examine the influence of the tip-cap shape, the tip-planform, the freestream Mach number, and the effect of centrifugal forces of rotation. Comparison of the numerical results with the		

20. ABSTRACT CONTINUED

available experimental data show good agreement for the surface pressures in the regions where the flow is attached or mildly separated. However, discrepancies exist in regions of massive shock-induced separation in transonic flow and in the immediate vicinity of the wing tip in subsonic flow. In general, a fairly good definition of the formation and roll-up of the tip vortex is demonstrated for all the cases considered here, subject to the coarseness of the grid in the far field. Finally, the calculated lift, drag and pitching-moment coefficients agree well with the experimentally determined values, where available. Alternate methods of simulating the hovering rotor flowfields in blade-fixed mode that have the same circulation distribution as hovering blade are explored. The results and discussion are presented.

Interaction of the tip vortices with a rotating helicopter blade have also been studied in the two-dimensional limit using a prescribed vortex approach. The important conclusions are that at the subcritical flow conditions, the time lag effects on the basic rotor blade and the three-dimensional effects appear to be negligible. Therefore, the numerical results are in good agreement with the experimental data. At the supercritical flow condition, however, the flowfield appears to be dominated by the presence of the shock waves, with strong indications of unsteady time lags in the shock wave motions and strengths and of important three-dimensional effects even for basic rotor flows in the absence of vortex interaction. The consequence of this is that the calculated results over predict the experimental data.

Summary

Thin layer Navier-Stokes equations are solved numerically for simulating the flow-fields of isolated wings and helicopter rotor blades with a particular emphasis on understanding the formation and roll-up of tip vortices in subsonic and transonic flows. Several test cases consisting of wings and rotor blades of different planforms have been considered to examine the influence of the tip-cap shape, the tip-planform, the free-stream Mach number, and the effect of centrifugal forces of rotation. Comparison of the numerical results with the available experimental data show good agreement for the surface pressures in the regions where the flow is attached or mildly separated. However, discrepancies exist in regions of massive shock-induced separation in transonic flow and in the immediate vicinity of the wing tip in subsonic flow. In general, a fairly good definition of the formation and roll-up of the tip vortex is demonstrated for all the cases considered here, subject to the coarseness of the grid in the far field. Finally, the calculated lift, drag and pitching-moment coefficients agree well with the experimentally determined values, where available. Alternate methods of simulating the hovering rotor flowfields in blade-fixed mode that have the same circulation distribution as hovering blade are explored. The results and discussion are presented.

Interaction of the tip vortices with a rotating helicopter blade have also been studied in the two-dimensional limit using a prescribed vortex approach. The important conclusions are that at the subcritical flow conditions, the time lag effects on the basic rotor blade and the three-dimensional effects appear to be negligible. Therefore, the numerical results are in good agreement with the experimental data. At the supercritical flow condition, however, the flowfield appears to be dominated by the presence of the shock waves, with strong indications of unsteady time lags in the shock wave motions and strengths and of important three-dimensional effects even for basic rotor flows in the absence of vortex interaction. The consequence of this is that the calculated results over predict the experimental data.

FOREWORD

The research reported in this document was performed for the U. S. Army Research Office under Contract DAAG29-85-C-0002 to JAI Associates, Inc., Mountain View, California with Dr. R. E. Singleton and Dr. Thomas L. Doligalski as Technical Monitors. Computational support was given by Dr. T. L. Holst, Chief of Applied Computational Fluids Branch at NASA Ames Research Center.

Drs. W. J. McCroskey, J. L. Steger, and T. L. Holst have provided helpful suggestions and guidance at various stages of this investigation. Dr. P. G. Buning, Mr. J. D. Baeder, and Mr. T. A. Edwards have also given help on several aspects of this program. Special thanks to these people for their help.

TABLE OF CONTENTS

SECTION	PAGE
SUMMARY.....	v
FOREWORD	vii
I GENERAL	1
II PART I: TIP VORTICES OF WINGS IN SUBSONIC AND TRANSONIC FLOWS...	2
III PART II: CALCULATION OF HOVERING ROTOR FLOWFIELDS	36
IV PART III: UNSTEADY, TWO-DIMENSIONAL BLADE-VORTEX INTERACTIONS...	71

GENERAL

This report describes a Navier-Stokes simulation procedure and presents results of flowfield and tip vortices for isolated wings and helicopter rotor blades and also the interaction of a vortex with a rotating blade. The contents of this report is divided in to three distinct parts. Each part describes in detail a separate but related physical problem; the common feature for these being a concentrated tip vortex and its influence. Part I describes a Navier-Stokes simulation of tip vortices for isolated wings and Part II concentrates on a single helicopter rotor blade and Part III describes the unsteady interaction of a concentrated vortex with a helicopter rotor blade in the two-dimensional limit. Each part is complete with introduction, solution procedure, results and discussion.

Part I

TIP VORTICES OF WINGS IN SUBSONIC AND TRANSONIC FLOWS

Nomenclature

B	=	semi-span of the wing
C	=	root chord of the wing
C_D	=	drag coefficient
C_L	=	lift coefficient
C_M	=	quarter-chord pitching-moment coefficient
C_P	=	pressure coefficient
$\hat{E}, \hat{F}, \hat{G}$	=	flux vectors
M_∞	=	free-stream Mach number
\hat{Q}	=	flow-field vector
\mathbf{q}	=	velocity vector
Re	=	Reynolds number
\hat{S}	=	viscous flux vector
u_∞	=	free-stream velocity
x, y, z, t	=	physical space coordinates
α	=	angle of attack, degrees
Γ_V	=	dimensionless strength of tip vortex, normalized by u_∞ and C
ξ, η, ζ, τ	=	generalized curvilinear coordinates

Part I

TIP VORTICES OF WINGS IN SUBSONIC AND TRANSONIC FLOWS

Introduction

The process of formation of a tip vortex and its subsequent roll-up in the downstream wake of a wing or helicopter rotor blade is a problem of fundamental importance in fluid mechanics, but one with important practical applications. The tip vortex evolves from a complex three-dimensional separated flow that is difficult to analyze. Despite a large number of theoretical and experimental studies, the present understanding of such flows remains essentially qualitative, especially regarding the detailed mechanics of vorticity transport from the viscous layers near the surface into the trailing concentrated vortex.

The hazards of concentrated vortices in the wakes of large aircraft are well known. Rotating blades, such as propellers and helicopter rotors, also generate complex vortical wakes that interact with the following blades. Such an interaction is responsible for the cause of unsteady aerodynamic loads which in turn affect performance, vibration and aeroacoustic characteristics. A detailed study of the formation and initial roll-up of such concentrated vortices and the dependence of these processes on the geometry of the blades is an important step toward altering the structure of these vortices and minimizing their adverse influence.

The recent numerical simulation of the viscous flow in the tip region of a transonic swept wing by Mansour¹ is a pioneering work, and Kaynak et al.² have extended this research to explore the details of three-dimensional shock-induced separation using a multi-block Euler/Navier-Stokes zonal method. The present study further extends the numerical simulation of this class of problems at both subsonic and transonic conditions, using this multi-block zonal method. Particular emphasis is placed on the flowfield in the tip region and the vortex formation process. The surface and flowfield topologies are presented for four different wing shapes, and the influence of the tip geometry and

wing planform is discussed. The numerical results are compared with the available experimental data.

Governing Equations and Numerical Scheme

The governing partial differential equations are the thin-layer Navier-Stokes and the Euler equations. The equations are transformed to the arbitrary curvilinear space (ξ, η, ζ, τ) while retaining strong conservation law-form to capture shock waves. The transformed equations written in generalized curvilinear coordinates are given by^{3,4}

$$\partial_\tau \hat{Q} + \partial_\xi \hat{E} + \partial_\eta \hat{F} + \partial_\zeta \hat{G} = \epsilon Re^{-1} \partial_\zeta \hat{S} \quad (1)$$

where

$$\begin{aligned} \hat{Q} &= J^{-1} \begin{bmatrix} \rho \\ \rho u \\ \rho v \\ \rho w \\ e \end{bmatrix}, \quad \hat{E} = J^{-1} \begin{bmatrix} \rho U \\ \rho u U + \xi_x p \\ \rho v U + \xi_y p \\ \rho w U + \xi_z p \\ U(e + p) - \xi_t p \end{bmatrix} \\ \hat{F} &= J^{-1} \begin{bmatrix} \rho V \\ \rho u V + \eta_x p \\ \rho v V + \eta_y p \\ \rho w V + \eta_z p \\ V(e + p) - \eta_t p \end{bmatrix}, \quad \hat{G} = J^{-1} \begin{bmatrix} \rho W \\ \rho u W + \zeta_x p \\ \rho v W + \zeta_y p \\ \rho w W + \zeta_z p \\ W(e + p) - \zeta_t p \end{bmatrix} \end{aligned} \quad (2)$$

and $\epsilon = 0$ for Euler equations, and $\epsilon = 1$ for thin-layer Navier-Stokes equations. The primitive variables of Eq. (1), *viz.*, $\rho, \rho u, \rho v, \rho w$ and e , are normalized by the free-stream reference quantities. The characteristic length and velocity scales are given by the wing root chord and the free stream sound speed, respectively.

The viscous flux vector \hat{S} , written here in the limit of thin-layer approximation, is given by

$$\hat{S} = J^{-1} \begin{bmatrix} 0 \\ K_1 u_\zeta + K_2 \zeta_x \\ K_1 v_\zeta + K_2 \zeta_y \\ K_1 w_\zeta + K_2 \zeta_z \\ K_1 (Pr^{-1}(\gamma - 1)^{-1}(a^2)_\zeta + ((q^2)/2)_\zeta) \\ + K_2 K_3 \end{bmatrix} \quad (3)$$

where

$$\begin{aligned} K_1 &= \mu(\zeta_x^2 + \zeta_y^2 + \zeta_z^2) \\ K_2 &= \mu(\zeta_x u_\zeta + \zeta_y v_\zeta + \zeta_z w_\zeta)/3 \\ K_3 &= u \zeta_x + v \zeta_y + w \zeta_z \\ q^2 &= u^2 + v^2 + w^2 \end{aligned} \quad (4)$$

The primitive variables of Eq. (1), viz., the density ρ , the mass fluxes $\rho u, \rho v, \rho w$ and the energy per unit volume e , are normalized by the free-stream reference quantities. The reference length and velocity scales are the chord of the rotor blade and free stream speed of sound respectively. Other nondimensional quantities appearing in the above equations are the Reynolds number Re and the Prandtl number Pr ; μ is the dynamic viscosity. The relations for the contravariant velocities U, V and W , the Jacobian of transformation J , and the metrics of the transformation $(\xi_t, \xi_x, \xi_y, \xi_z), (\eta_t, \eta_x, \eta_y, \eta_z)$ and $(\zeta_t, \zeta_x, \zeta_y, \zeta_z)$ can be found in Ref. 4.

The velocity components u, v, w and the pressure, p , are related to the total energy per unit volume, e , through the equation of state for a perfect gas by

$$p = (\gamma - 1)(e - \frac{\rho}{2}(u^2 + v^2 + w^2)) \quad (5)$$

The numerical code which solves these equations, called ARC3D,⁴ was adapted by Holst et al.⁵ and Flores⁶ to develop the transonic Navier-Stokes (TNS) multi-block zonal algorithm. This code retains all the important features of the ARC3D code and in addition has the advantage of dealing with multiple-blocks. The details of the development of this 4-block version of the TNS wing code and improvements to enhance its efficiency for multiple zones are described in the papers of Holst et al.⁵ and of Flores⁶. In addition

to the example solutions for isolated wings discussed in these two papers, Kaynak et al.³ have reported further refinements to this code to analyze the flow topology of shock induced separated flows on wings in transonic flows. The current version of this 4-block scheme is mainly used for computing the flow fields of isolated wings, with or without wind-tunnel walls.

The five important features of the TNS code are: (1) the thin-layer Navier-Stokes equations and the Euler equations are solved in strong conservation-law form to capture shock waves; (2) the convergence procedure is significantly accelerated over the standard ARC3D code for one-block,⁴ because the present scheme solves the Euler equations over a significant part of the flow domain; (3) there are two numerical options available for solving the equations. One is based on the standard ADI algorithm of Beam and Warming⁷ which solves the block-tridiagonal matrices along each coordinate direction. The other is based on the diagonalized algorithm of Pulliam and Chaussee⁸ which solves a set of five scalar pentadiagonal matrices along each coordinate direction; (4) the diagonal algorithm has been implemented with two options of variable time-step philosophies to accelerate the convergence rate of the numerical scheme, *viz.*, one that scales the marching time-step with the local Jacobian as suggested by Srinivasan et al.⁹ and the other that scales the time-step using a combination of the Jacobian and local solution variation;^{4,6} (5) the code is vectorized for the Cray-XMP and Cray-2 supercomputers.

Both the numerical codes (TNS and ARC3D) use the standard second-order- accurate central differencing to construct the appropriate spatial differencing scheme. The diagonal version, which is used in the present study to calculate steady-state solutions, uses fourth-order-accurate smoothing operators on the implicit and explicit sides of the numerical algorithm for controlling nonlinear stability of the numerical scheme. In the present calculations a turbulent boundary layer is assumed for the entire wing, and the Baldwin and Lomax algebraic turbulence model ¹⁰ is used to calculate the turbulent eddy viscosity. Although this model has some limitations, it has been effectively applied to a variety of two- and three-dimensional flow problems involving mild separation.

Grid Generation and Data Management

The details of the grid-generation scheme and the data management system are described in Ref. 5. For the sake of completeness, the important steps that are necessary to generate a working finite-difference grid are described here. First, a coarse grid encompassing the entire flow field is generated using the parabolic grid-generation scheme of Edwards.¹¹ This single-block grid has an H-grid topology in both the spanwise and chordwise directions. The grid is further subdivided into four zones by means of the zoning algorithm in the TNS code. Thus the complete flow domain is divided into four blocks. Figure 1 shows a pictorial view of one such grid topology for a low aspect ratio wing. In this view, for clarity, only the grid at the symmetry plane of the wing is shown. The coarse outer (inviscid) grid, marked as block (1), is shown in white, the finer inviscid grid, marked as block (2), is shown in red. The two yellow blocks adjacent to the wing and on either side of it, marked as blocks (3) and (4), are the viscous zones that have fine clustering in the normal direction to resolve the boundary layer, in the stream-wise direction at the leading-edge and trailing-edge regions, and in the span-wise direction at the wing tip region to resolve the tip vortex. The inviscid grids also have appropriate clustering like-wise.

Most of the calculations were done with a default grid consisting typically of over 40,000 grid points in each of the four zones. For such a grid the wing tip was assumed to have a bevelled (or a triangular) tip-cap. Although the grid geometry for each wing discussed here depended on the aspect ratio of the individual wing geometry, the spanwise grid spacing in the wing tip region and the spacing in the normal direction to the wing surface were kept the same for all the wings, *viz.*, 0.015C and 0.15C in the coarse grid. The viscous blocks (of size 0.15C) had 25 finely clustered grid points in the normal direction for all the wings with the spacing at the surface equal to $1 \times 10^{-5}C$.

To examine the effect of the tip-cap shape, a squared (flat) tip and a rounded (body of revolution) tip were also considered for the rectangular wing in subsonic flow. In order to get a good definition of these tip profiles, the spanwise clustering had to be increased

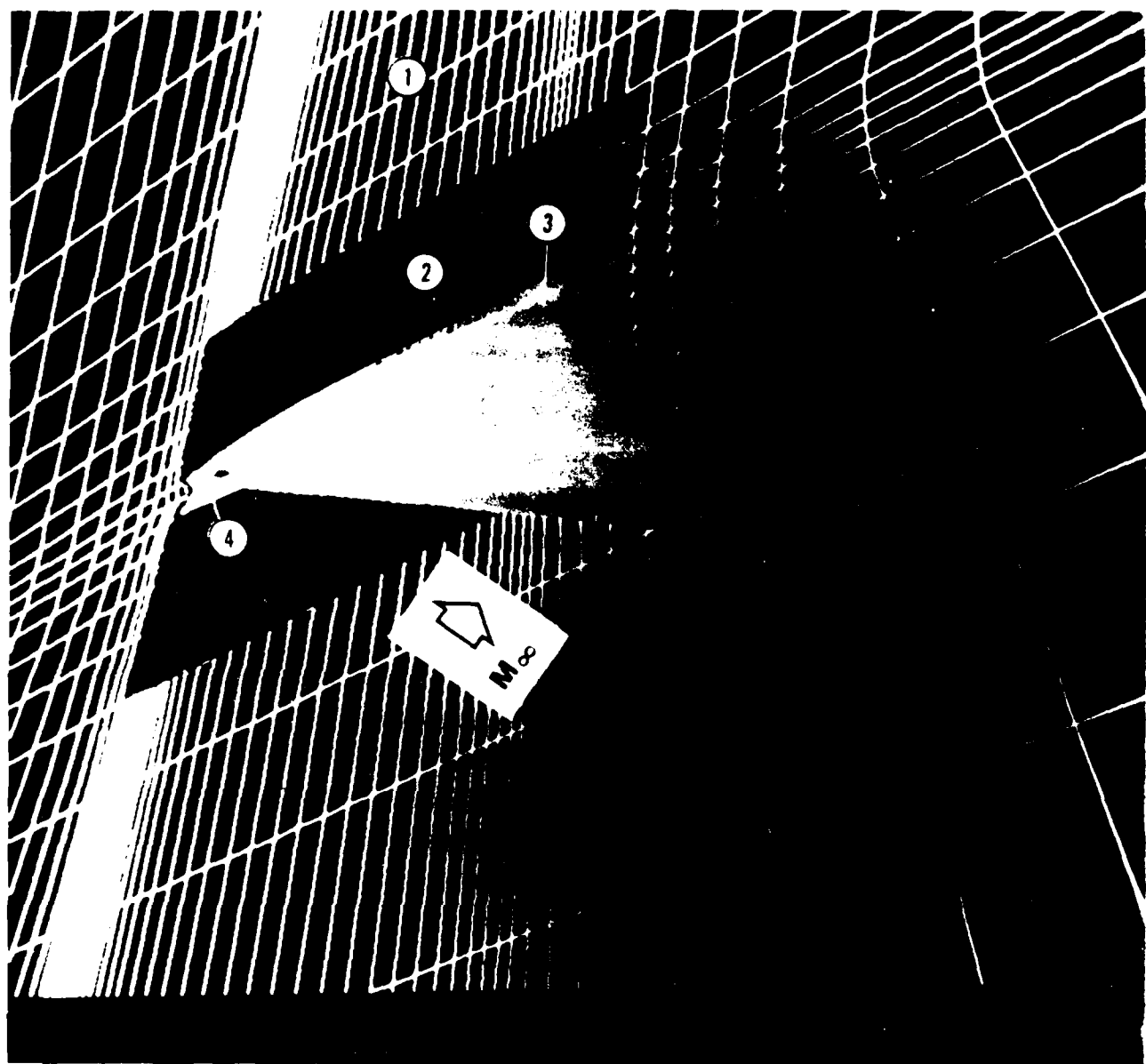


Fig. 1. Typical zonal grid topology. Outer zones identified as 1 and 2 are inviscid zones, inner zones 3 and 4 are viscous zones.

near the tip region. These grids had nearly 90,000 grid points in each zone. The spacing of the grid at the wall in the normal direction was the same as mentioned before, but at the tip-cap it was reduced to 0.004 in the spanwise direction.

The data management strategy has been discussed by Holst et al.⁵ and also by Kaynak et al.² In brief, the base grid, which is usually generated outside the TNS code, is "read in" first and this grid is further divided into appropriate zones by the "Zoner" code. Once this is done, the flow solver is initiated. The iteration procedure starts in the outer inviscid zone or block, and proceeds into the inner viscous blocks. The information necessary to update the boundary conditions at the zonal interface is found from the neighboring zones through a series of one-dimensional linear interpolations. Such a scheme lends itself to a conservative treatment of the boundaries and thus captures distortion-free-movement of discontinuities across the boundaries.

In the solution procedure, only the information necessary to solve each zone resides at any one time in the main memory of the Cray-XMP computer. The information of zones which are not being computed is temporarily stored on the Solid State Device (SSD). The use of SSD frees the main memory of the space otherwise taken by the data stored on the SSD, and enables the use of (allowable) maximum number of grid points for the flow field. Also, the use of SSD reduces the I/O wait time significantly.⁶

Boundary Conditions

Since the TNS code is a multi-block zonal algorithm, there are two types of boundaries where conditions have to be specified; *viz.*, (1) the physical boundaries, such as inflow, outflow, and solid surfaces; and (2) the zonal boundaries across which all flow quantities must be continuous. All the boundary and zonal interface conditions are applied explicitly.

At the far-field boundaries, which are typically 6-10 chords away from the wing, free-stream values are specified for all the flow quantities. At the outflow boundaries, zeroth-order extrapolation is used from the grid interior. At the symmetry plane, a

zeroth-order extrapolation is used for the density and a first-order extrapolation is used for the x-component and the z-component of velocities while setting the spanwise velocity component to zero to force symmetry. A first-order extrapolation is also used for the pressure and the energy is calculated from the equation of state. At the surface of the wing, a no-slip condition is used for the velocity components and the pressure is calculated by solving the normal momentum equation at the surface. In the spirit of thin-layer approximation, the normal momentum equation reduces to $dp/dn = 0$, where n is the local normal to the surface. Density is determined by assuming an adiabatic wall condition. Given the pressure, p , and the density, ρ , at the wall, the total energy, e , is determined from Eq. (5). The details of the zonal interface boundary conditions are described in Refs. 2 and 5.

Results and Discussion

In this section, numerical results are presented at subsonic and transonic flow conditions for four isolated wing configurations. These results are compared with the available experimental data. The different flow conditions and the wing geometries considered consist of: (1) a rectangular wing with an aspect ratio (based on semi-span) of 2.5 without twist or taper, in a uniform flow of $M_\infty = 0.17$ at $\alpha = 5^\circ$ and $Re = 2 \times 10^6$; (2) a typical fighter aircraft wing with twist and taper and an aspect ratio of 0.83 in a uniform flow of $M_\infty = 0.9$ at $\alpha = 5^\circ$, and $Re = 6.8 \times 10^6$; and (3) two wings with exotic tip shapes typifying helicopter rotor blades, with aspect-ratios of 5.0, at $M_\infty = 0.85$, $\alpha = 5^\circ$ and $Re = 8.5 \times 10^6$. The planforms and the surface grids of these wing geometries are shown in Fig. 2.

Rectangular Wing in Subsonic Flow

The rectangular wing configuration and the subsonic flow conditions considered here corresponds to the experimental test case of Spivey and Moorhouse ^{12,13} with the above shown test conditions. The wing section is made up of an NACA-0015 airfoil and has no twist or taper. Although in their experiments Spivey and Moorhouse chose a wing

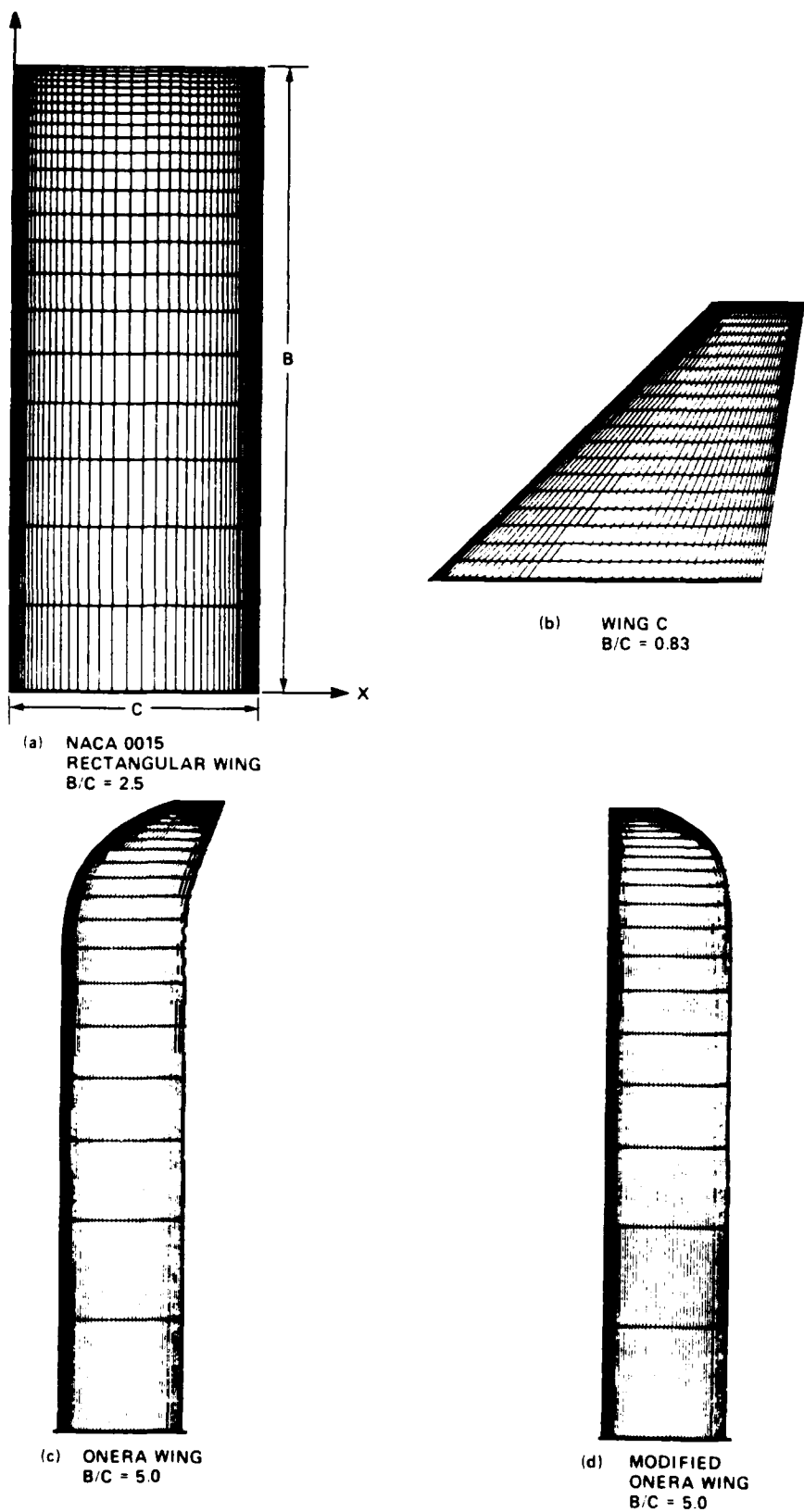


Fig. 2. Planforms and surface grids of the four test wings.

with only a square (or flat) tip configuration, the present calculations consider three different tip-cap configurations to examine the influence of the tip-cap on the tip vortex formation and its subsequent roll-up process. A cross-sectional view of these tip configurations is shown in Fig. 3 and consist of a) a squared (or flat) tip-cap, and b) a rounded (or body of revolution) tip-cap, and c) a bevelled (or triangular) tip-cap. The surface grids and the flow field grids were generated using a parabolic solver of Edwards¹¹ as mentioned before. An H-H grid topology was generated by this method for the three tip configurations, and Fig. 3 shows this $H - H$ grid topology in the tip region for the square and triangular tip-caps. The hyperbolic grid generator of Steger and Chaussee¹⁴ was also used to construct spherically-warped O-O grid topologies for the round tip and for a super-ellipse approximation to the square tip (ratio of major axis to minor axis equal to 15); this O-O grid is sketched in Fig. 3 for the round tip. It should be noted that solutions were computed for both H-H and O-O grid topologies. While the H-H grid was used with the TNS code, the O-O grid topology was used with one-block flow solver of Ying et al.¹⁵ This flow solver, called SF3D, is also a derivative of the ARC3D code⁴ and has the same features of ARC3D code except it uses upwinding in one of the coordinate directions and a partially flux-split algorithm. The flow field computations were performed on the Cray-2 supercomputer with this code.

A representative surface grid for this wing (with bevelled tip-cap) is shown in Fig. 2a; it has 96 points (48 each on upper and lower surfaces) in the streamwise direction and 23 points along the span. This default grid has approximately 40,000 grid points in each of the four zones. The round and square tip-cap configurations, in contrast, have a much better surface definition in the tip region with 57 points along the span but with the same number of streamwise points. This translates into about 90,000 grid points for each of the four zones. Typical computational times for the steady state calculations, for a four-order drop in residuals with the TNS code, was of the order of 5-12 hours on the Cray-XMP supercomputer depending on the grid size. The single-block grids for these configurations (used with SF3D code and Cray-2 supercomputer), on the other hand, had 155 points in the periodic (streamwise) direction, 66 points in the spanwise

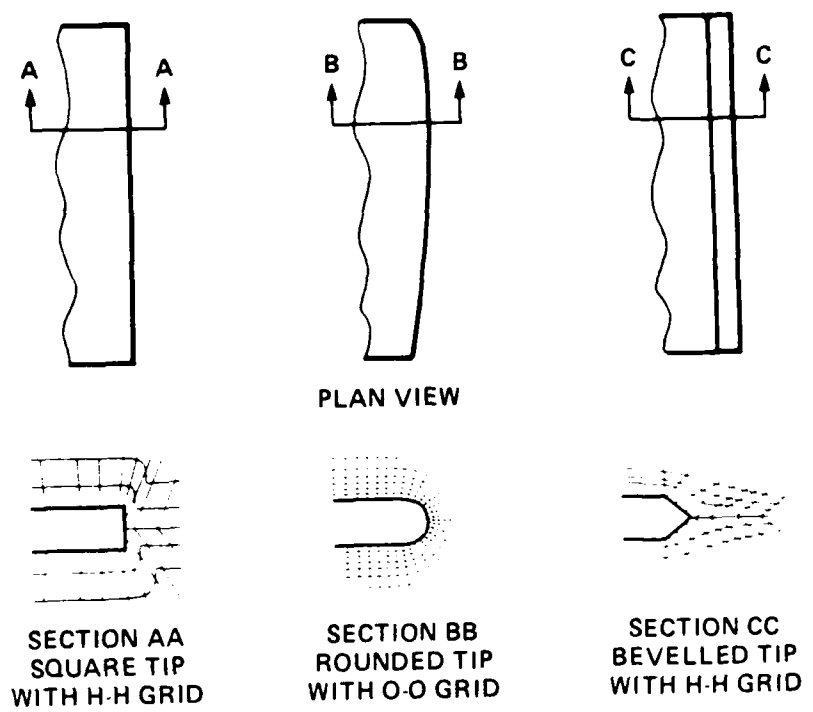


Fig. 3. Schematic of tip planforms and tip-cap shapes for NACA 0015 rectangular wing.

direction, and 66 points in the normal direction.

Typical results for this wing with different tip-cap options are shown in Figs. 4-7. Figure 4 shows the computed surface pressure distributions at several spanwise stations compared with the experimental data.^{12,13} The results shown here for the inboard spanwise stations are essentially the same for all the tip-cap options and have a typical two-dimensional attached flow behavior and these are in very good agreement with the experimental data. The leading-edge suction peak and local lift coefficient decrease monotonically from root to tip, as expected due to the induced downwash of the tip vortex and wake vortex sheet. Although the three different tip-caps produce very different flow fields in the tip region, the good agreement of the surface pressure distributions for about 90% of the span, as shown in Figs. 4a-c, suggests that the influence of the tip-caps is restricted to the outer 5-10% of the span.

The flow field in the tip region appears very different for each of these tip-caps, as mentioned above. For example, the chordwise surface pressure data for the square tip wing of Refs. 12-13, shown in Fig. 5, show two suction peaks in the tip region, besides the leading-edge suction peak. These are associated with the primary and secondary tip vortices created slightly inboard of the sharp edge on the upper surface of the wing; the primary peak occurs at near the midchord and the secondary peak is farther aft (towards the trailing edge) and more inboard. The presence of two peaks in the tip region has also been observed in the experiments of Triebstein¹⁶ for the square tip wing. The interaction of the primary vortex with the surface boundary layer is responsible for the creation of the counter-rotating secondary vortex similar to that observed on sharp edged delta wings.¹⁷

The calculated surface pressure distributions in the tip region of the rectangular wing with different tip-caps is compared to the experimental data of square tip wing.^{12,13} As seen here for the square tip configuration, the present calculations reproduce very well the evolution and disappearance of the suction peak due to the primary vortex and the results are in good qualitative agreement with experiments. The location of the

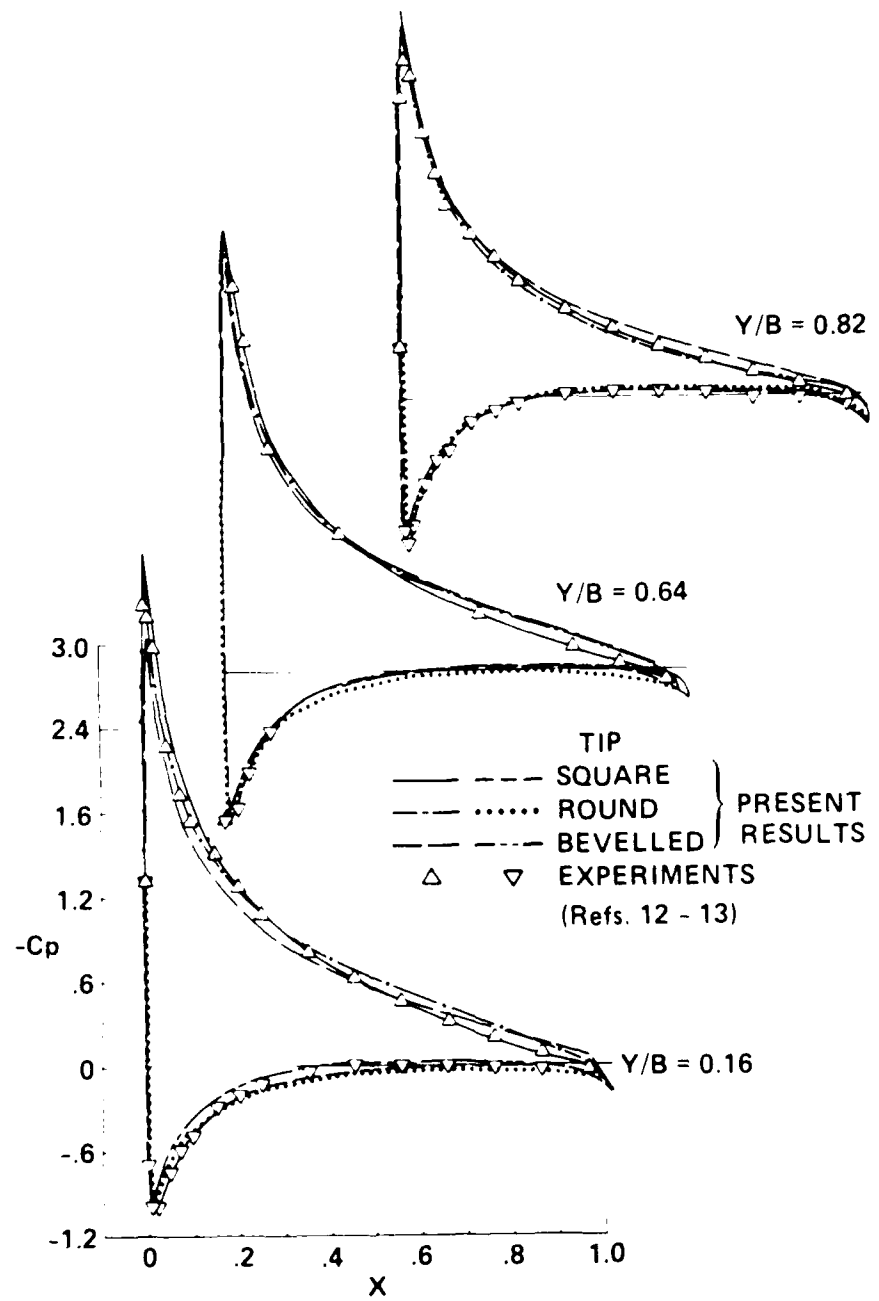


Fig. 4. Calculated surface pressure distributions for the rectangular wing with different tip-caps compared with experimental data. $M_\infty = 0.17$, $\alpha = 11.8^\circ$, and $Re = 2 \times 10^6$.

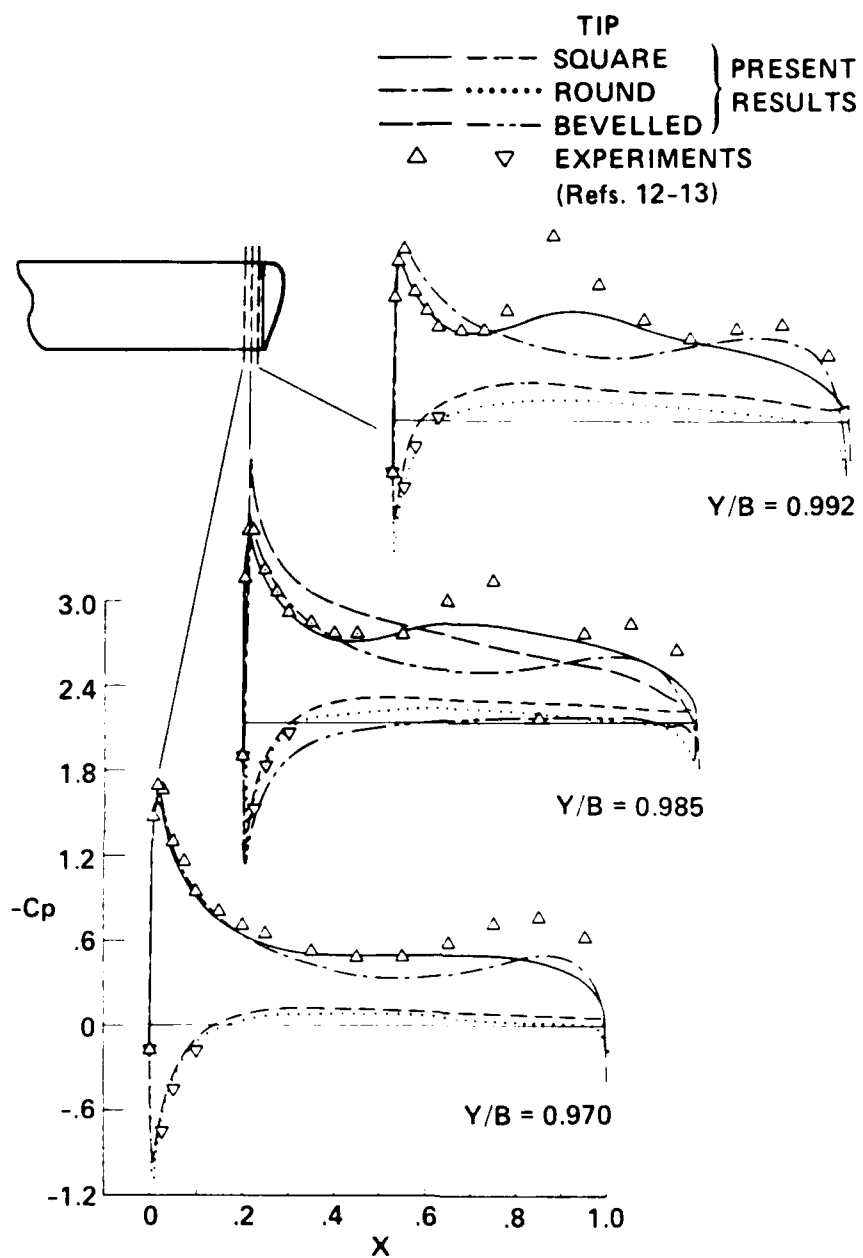


Fig. 5. Surface pressure distributions in the tip region for the rectangular wing with different tip-caps. $M_\infty = 0.17$, $\alpha = 11.8^\circ$, and $Re = 2 \times 10^6$.

primary vortex is reasonably well predicted. The suction under both the primary and the secondary vortex, on the other hand, appears weaker compared to the experimental value and in this part of the pressure distribution plots the comparison is only qualitatively good as noted earlier. Also, the separation bubble on the face of the tip, as visualized in the water tunnel tests of Thompson,¹⁸ was not resolved. No dramatic improvement was observed in these results when the grid resolution was increased by 50% in the tip region or even when the grid topology was changed from H-H to O-O type. Also, a laminar calculation for this case did not reproduce the suction peak due the secondary vortex. The possible reasons for this could be the assumption of thin layer equations, the use of a simple turbulence model, and inadequate grid resolution.

Figure 5 also shows the surface pressure distribution for the round-tip wing. In contrast to the observation of two suction peaks for the square tip-cap wing, the rounded tip-cap produces only one suction peak, in agreement with the observation made by Triebstein.¹⁶ The location of this suction peak is outboard and further aft in comparison to the primary suction peak location of the square tip wing. This implies that the vortex formation is delayed toward the trailing edge for the rounded-tip wing unlike the wing with squared-tip, for which the process seems to have started almost from the leading edge region because of the larger extent of separated region. Also, because the extent of the suction peak is narrower in the spanwise direction, the vortex appears to be more tightly wound (smaller core size) than the square tip case.

In contrast, Fig. 5 shows no obvious suction peaks for the bevelled tip-cap configuration. The flow in the tip region for the bevelled-tip wing thus appears to be very different from that of the square tip wing, although both these tip geometries have a tendency to separate the flow right at the leading edge. For the square tip case, the flow going around the wing tip from the (high pressure) lower surface to the (low pressure) upper surface seems to delay the onset of separation to slightly downstream of the leading edge region. For the bevelled tip wing, however, the separation point is fixed right at the sharp point of the leading edge of the tip. Further examination of this tip-cap

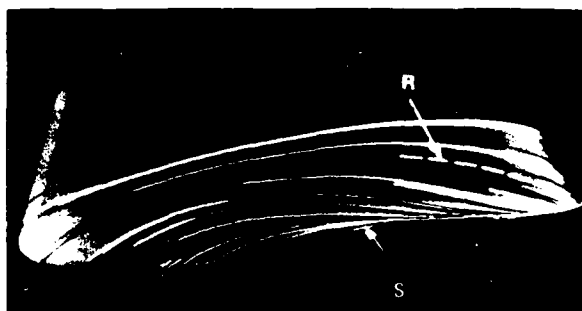
geometry has revealed that its shape degenerates into a zero-thickness sharp point at the leading and trailing edges. The sharp corner at the wing tip leading edge is responsible for producing a larger separated region than the square tip wing would produce and thus mask the suction peak that otherwise would exist due to the primary vortex. This observation is in good qualitative agreement with the water tunnel flow visualization studies of Thompson.¹⁸ As a consequence the pressure field for this tip-cap does not show any indication of the tip vortex presence from the surface pressure distributions. Otherwise these results are in overall agreement with the results of other tip-caps and of the experiment for the square tip at 97% span station as shown in Fig. 5 for the lower surface and up to about the midchord on the upper surface.

Figure 6 shows the details of the surface "oil flow" pattern in the tip region for these three tip-caps. (Computationally the surface oil flow picture is generated by releasing fictitious fluid particle tracers at one grid point above the surface and restricting the paths of these particle tracers to lie in that plane.) An examination of these figures reveal that the square tip, Fig. 6c, produces the most complex separated flow pattern of the three tip-caps considered here. The rounded tip-cap, Fig. 6b, produced the least separation and the bevelled tip-cap, Fig. 6d, produced the most. Comparison of the experimental surface oil flow for the rounded-tip of Fig. 6a (reproduced from the ongoing experiments at the Army Aeroflightdynamics Directorate at NASA Ames Research Center) with the computed flow of Fig 6b shows excellent agreement in this region. The separation and reattachment lines observed in the experiment are well predicted. However, for the bevelled tip-cap geometry the extent of separation region on the wing is more pronounced than is apparent from the experimental pressure contour plot of Chigier and Corsiglia¹⁹ for the square-tip wing, indicating that the bevelled tip-cap, first thought to mimic the experimental square tip, is really different and is neither a near-squared nor a near-rounded tip.

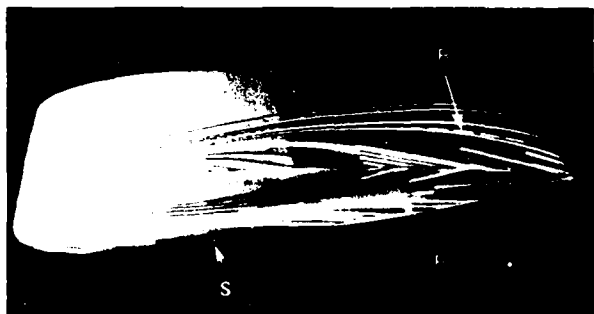
The close-up views of the formation and lift-off of the tip vortex for the round and square tips are shown in Fig. 7. These are constructed by releasing unrestricted fluid



a) ROUND TIP-EXPERIMENT



b) ROUND TIP-CALCULATIONS



c) SQUARE TIP



d) BEVELLED TIP

Fig. 6. Computed and experimental surface particle flow pattern in the tip region. $M_\infty = 0.17$, $\alpha = 11.8^\circ$, and $Re = 2 \times 10^6$. The symbols S and R denote separation and reattachment lines.



(a) ROUND TIP



(b) SQUARE TIP

Fig. 7. Formation and lift-off of the tip vortex for the rectangular wing with a) Round tip and b) Square tip; $M_\infty = 0.17$, $\alpha = 11.8^\circ$, and $Re = 2 \times 10^6$.

particle tracers at several locations along the chord and span and at different heights from the surface of the wing on both upper and lower surfaces. It is seen from this that the formation process of the tip vortex consists of the braiding of fluid particle tracers released from both upper and lower surfaces of the wing. The fluid particles released on the lower surface (high pressure side) smoothly cross over the wing tip and mix with the particles released on the upper surface and braid into each other. This tightly braided bunch of fluid particles define a tip vortex that is distinct from the rest of the wake vortex sheet. While the braiding process is still in progress, the vortex lifts off the surface, and as it rolls up it also starts rolling inboard of the wing tip. Further downstream of this, it continues to roll inboard and stays distinctly above the shed wake vortex sheet. The formation process of the tip vortex for both the round tip and the square tip wing begins well before the mid-chord position as shown in Fig. 7. Because of the small extent of separation associated with the smooth curvature of the round tip-cap, the lift off of the vortex from the surface is delayed well into the trailing edge region as apparent from Fig. 7a. In contrast, the square tip-cap, for which the extent of separation is larger, produces a tip vortex that lifts off from the surface around the mid-chord as shown in Fig. 7b. It appears that the round tip produces a tightly braided tip vortex compared to the square tip. Also the distinct separation of the tip vortex from the wake vortex sheet is clearly seen in these figures. For the square tip wing, the primary and secondary vortices seem to merge into one distinct tip vortex in the downstream wake.

The lift, drag, and quarter-chord pitching-moment coefficients calculated for the square tip wing are 0.762, 0.0886, and -0.004, respectively. This compares well with the measured data of 0.763, 0.0868, and -0.00843 for the lift, drag, and pitching-moment coefficients, respectively (from the tabulated data of experiments of Spivey and Moorhouse (Refs. 12-13) provided by U. S. Army Aeroflightdynamics Directorate). From the lift coefficient, the approximate strength of tip vortex can be estimated using the definition of lift-equivalent vortex strength as 0.38. (Note the vortex strength is nondimensionlized by the free-stream velocity and the chord of the wing.)

Consistency of the vortical model was checked by comparing the value of $C_L/2$ with the line integral of the velocity vector \mathbf{q} over a closed path \mathbf{s} enclosing the tip vortex, *viz.*,

$$\Gamma_V = \oint_{\mathbf{s}} \mathbf{q} \cdot d\mathbf{s} \quad (6)$$

The result of such a line-integral over a path big enough to enclose the tip vortex at several x -stations behind the wing gave a range of values from 0.37-0.41, depending on the size of the integration path around the vortex. The larger value corresponds to the case of the line-integral path extending all the way to the wing root in the y -direction and extending to the limits of the grid in z -direction. The extent of this path is expected to include the contribution from the wake vortex sheet also.

Swept Tapered Wing in Transonic Flow

Transonic calculations were performed on an advanced technology wing, called Wing C, which has been extensively studied both computationally^{1,2} and in wind-tunnel experiments.^{20,21} Its planform and the surface grid are shown in Fig. 2b. It is a low aspect-ratio (equal to 0.83 based on the root chord) wing which is made up of supercritical wing sections, with a twist angle of 8.17 degrees, a taper ratio of 0.3 and a leading-edge sweep of 45 degrees. As noted earlier, Mansour,¹ in a pioneering but limited study, attempted to simulate the flowfield in the tip region including tip vortex formation for this wing in a free-stream Mach number of 0.82 and at 5 degrees angle of attack. Recently Kaynak et al.² have presented extensive computational results for this wing for a range of Mach numbers using the TNS code. Whereas the study of Ref. 2 concentrated on analyzing the flow topology, the present study specializes in the flow in the vicinity of the wing tip, and in particular concentrates on the tip vortex phenomenon.

The freestream conditions for the present computations are $M_\infty = 0.9$, $\alpha = 5^\circ$, and $Re = 6.8$ million based on the mean aerodynamic chord. As before, the computational grid was generated first by a grid solver¹¹ with sufficient grid resolution in the wing tip

region so as to resolve the tip vortex. The interior grids were generated within the TNS code by the Zoner program. The CPU time for a fully converged solution was about 5 hours for this case, which is highly transonic and has a shock-induced flow separation on the upper surface of the wing. Typical results of surface pressures are shown in Fig. 8 compared with the experimental data of Keener.²⁰ The agreement is very good over parts of the wing which do not have massive shock-induced separation and the results are in general agreement with those of Ref. 2. With additional numerical experiments with the turbulence model and input from experiments for specifying the inflow and outflow boundary conditions, Kaynak and Flores²² have recently demonstrated, with this code, that it is possible to model more accurately the shock-induced separation region also. However, such an exercise was not undertaken in the present investigation.

Tip vortex formation and subsequent roll-up was visualized as before by releasing fluid particle tracers at different locations along the chord and span and at various heights from the wing surface. Figure 9 shows some of the flow details for this wing, such as the λ -type shock wave and shock-induced separated flow, and a view of the tip vortex where the initial formation and subsequent roll-up process are clearly seen. As before, the tip vortex stays distinctly above the wake vortex sheet. Part of the separated flow from the shock-induced separated region lifts up from the wing surface and merges in to the flow in tip region. The fluid particle tracers from this region get braided into the particle paths crossing over the tip from the high-pressure region of the wing lower surface, and together they separate out into the tip vortex and stay distinctly apart from the rest of the vortex sheet.

The view in Fig. 9 demonstrates clearly the way the vortex rolls inboard in the downstream wake after leaving the surface of the wing. The shape and strength of the tip vortex are apparent from the vorticity contours shown here at several x-locations. These contours are shown as slices taken across the tip vortex in the y-z plane. In these, the vorticity magnitude increases in the order of blue-yellow-red color. As the tip vortex is getting diffused in the far-field coarse grid,⁹ the magnitudes of the vorticity contours

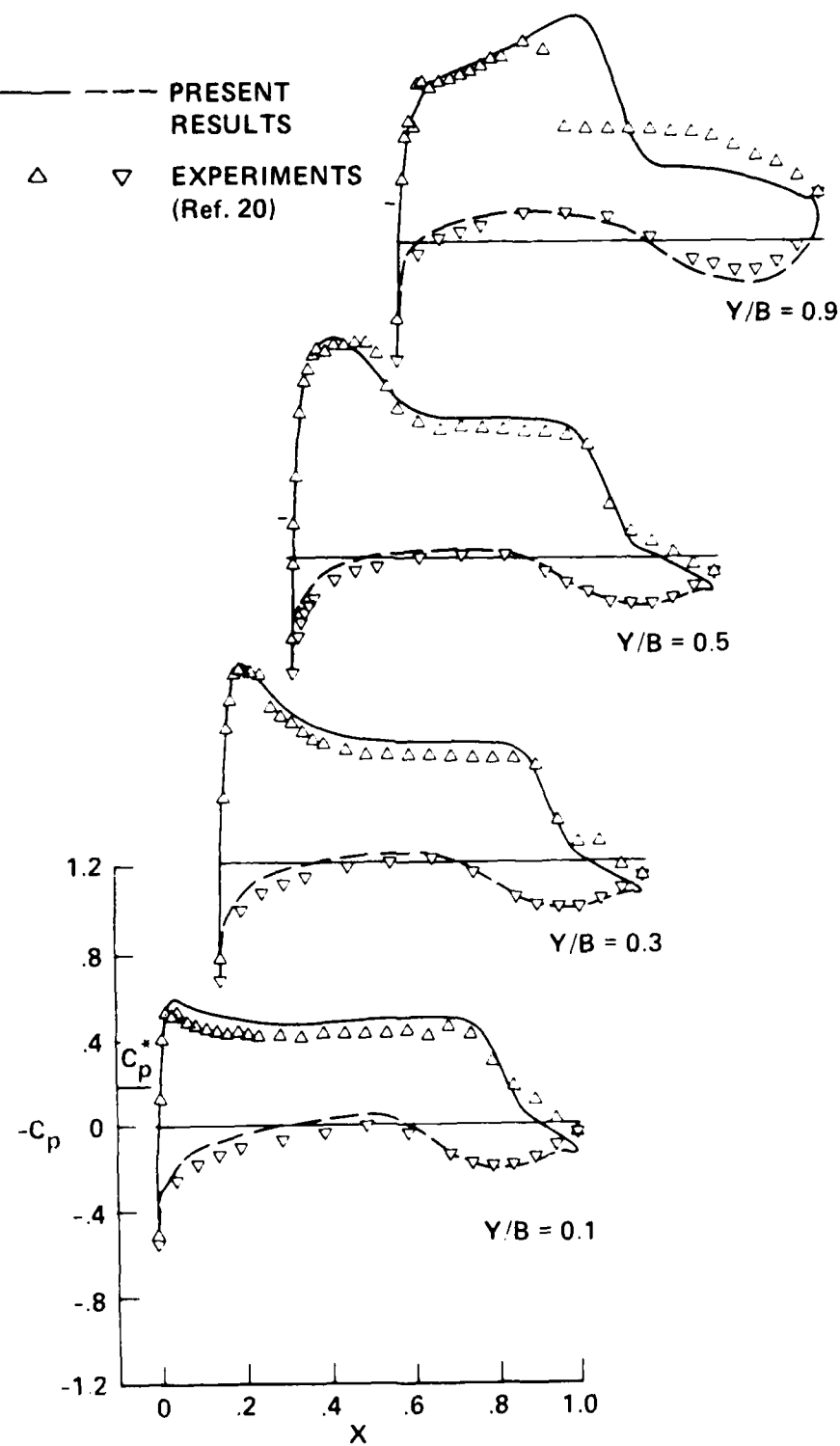


Fig. 8. Calculated and experimental surface pressure distributions for the swept tapered Wing C; $M_\infty = 0.90$, $\alpha = 5^\circ$, and $Re = 6.8 \times 10^6$.

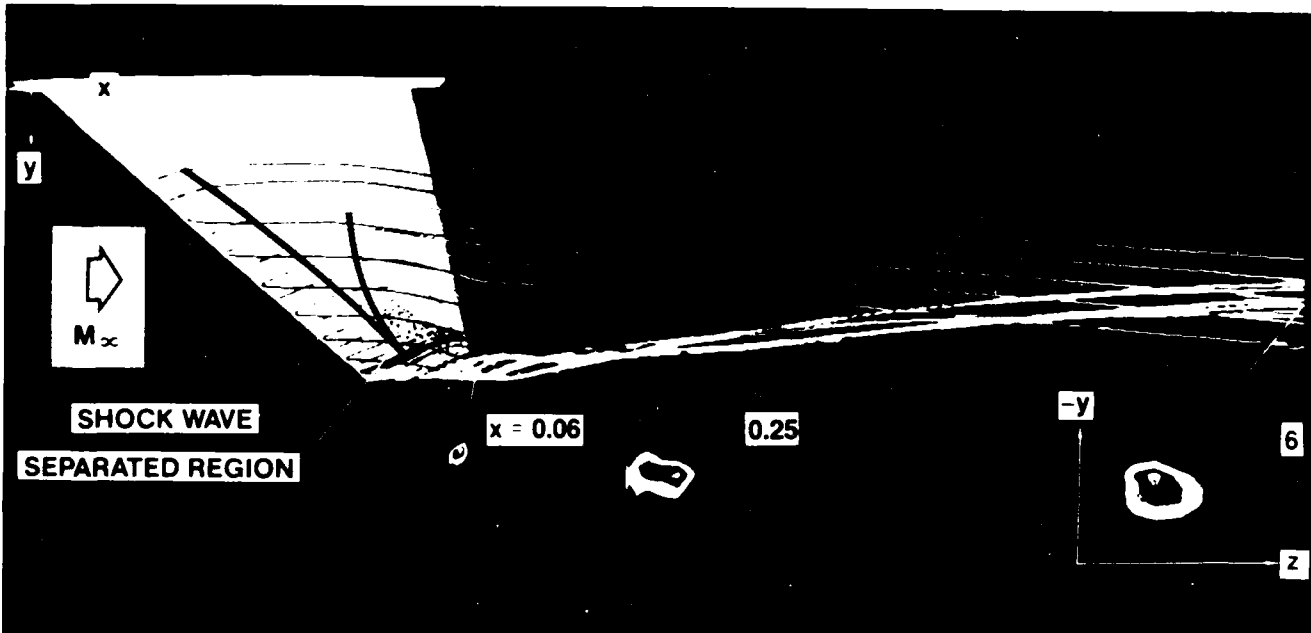


Fig. 9. Shock wave, separated region, vorticity contours, and farfield view of the tip vortex for Wing C.

decrease and the the cross-section of the tip vortex appears to have stretched according to the grid-cell aspect ratio. But the line-integral of the velocity vector around a closed path surrounding the tip vortex approximately remains constant as long as the integration path is large enough to contain the tip vortex. For this wing, the calculated values of the aerodynamic coefficients were $C_L = 0.361$, $C_D = 0.0347$, and $C_M = -0.146$. The strength of the vortex determined from the line-integral method yielded a value between 0.17 and 0.185, depending on the size of the integration path around the tip vortex. The smaller value includes the vortex sheet in the wake and therefore corresponds to the larger path of the integral (usually extending to the symmetry plane in the y-direction and to the boundaries in the z-direction).

ONERA Wing in Transonic Flow

This wing has an aspect-ratio of 5 and represents a typical helicopter rotor blade.²³ The geometry for this wing has a combination of rectangular wing and swept-tip wing. The wing is made up of three special airfoil sections ranging in thickness from 12 % to 6 % from root to tip. The wing has a constant chord up to about 70% of the span station and tapers toward the tip. The surface grid for this wing has only 23 spanwise stations (for the default grid size) in the fine Euler and the viscous zones and hence is very sparse in this direction, as shown in Fig. 2c. For this wing in a uniform free-stream of $M_\infty = 0.85$, $\alpha = 5^\circ$, and $Re = 8.5$ million (based on the root chord), computations were carried out to generate a steady-state solution.

Figure 10 shows the computed surface-pressure distributions for several spanwise stations along the wing. Examination of these indicate the presence of a strong shock wave on the upper surface which produces a complex large scale separation. The leading edge spikes that are seen in the pressure distributions are due to the poor leading edge definition of the wing. This was verified independently by making two-dimensional calculations for several sections of the wing span with refined leading edge definition. The surface flow pattern for this configuration shows important topological features of a complex separated flow and an outward spiralling vortex emanates from this separated

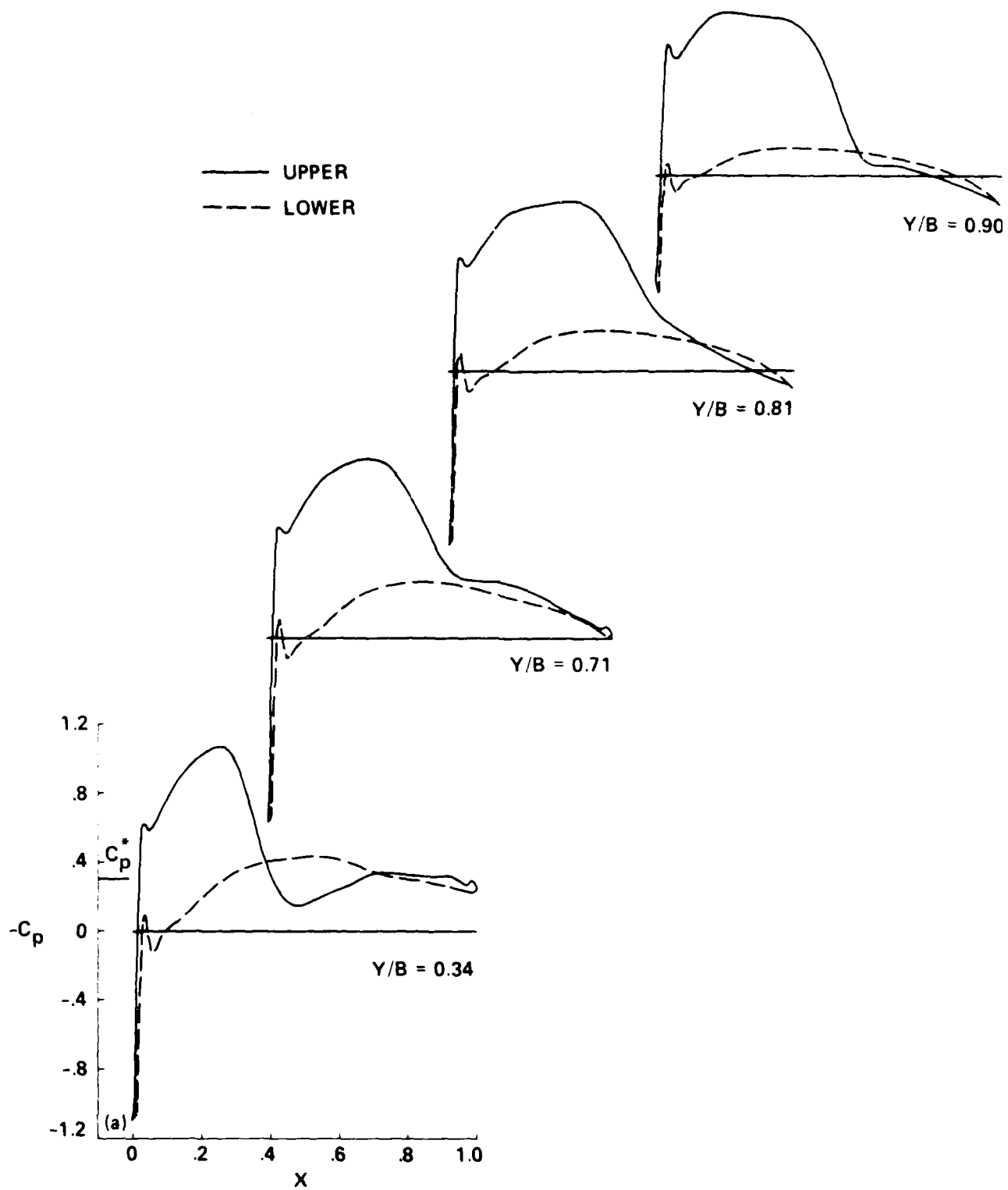


Fig. 10. Surface pressure distributions for the swept-tip ONERA wing. $M_\infty = 0.85$, $\alpha = 5^\circ$, and $Re = 8.5 \times 10^6$.

region.²⁴

Figures 11-12 show two views of the tip vortex for this wing. The initial formation process of the vortex and lifting off from the wing surface is shown in Fig. 11. The cross flow, due to the swept-tip shape of the wing, enables the fluid particles released in the vicinity of the tip to merge together and braid into a distinct tip vortex. Also, the fluid particles released on the high-pressure side of the wing (lower surface) at the tip cross over to the low-pressure side (upper side) by wrapping around the wing tip and braid into the swirling tip vortex. For this tip geometry, the intricate braiding of fluid particle tracers appears to produce a much tighter vortex than for any of the other cases considered. Figure 12 shows the far-field view of this tip vortex. The lift off of the tip vortex from the wing surface and then the roll-up in the downstream wake and the inward migration are clearly evident from this photograph. Also shown here is the strong transonic shock wave and associated massive shock induced separation and reattachment (shown as dashed line parallel to the trailing edge). In addition, the vorticity contours drawn in the y-z planes through the tip vortex at several x-locations behind the wing suggest approximate vortex strengths and shapes at these locations. As observed before, the vorticity levels of the contours decrease in the downstream coarse-grid region of Block 1, and the shapes of these contours (and hence the shape of the tip vortex) get stretched in the pattern of the grid geometry.

The lift, drag, and the pitching-moment coefficients for this wing are respectively $C_L = 0.26$, $C_D = 0.061$, and $C_M = 0.002$. It should be pointed out here that this particular configuration is not designed to operate in a uniform free stream, but rather to operate as a helicopter blade for which the speed increases from the root to the tip in a linear fashion. Therefore it is not surprising to note a slightly positive (destabilizing) pitching-moment for this wing. Based on the definition of lift-equivalent vortex strength, the nondimensional tip vortex strength for this wing is 0.13. Also, the value of Γ_V determined from the line-integral of the velocity vector around a closed path surrounding the vortex and at several x-locations in the wake is in the range between 0.12 – 0.14 depending on



Fig. 11. Tip region of the ONERA wing.

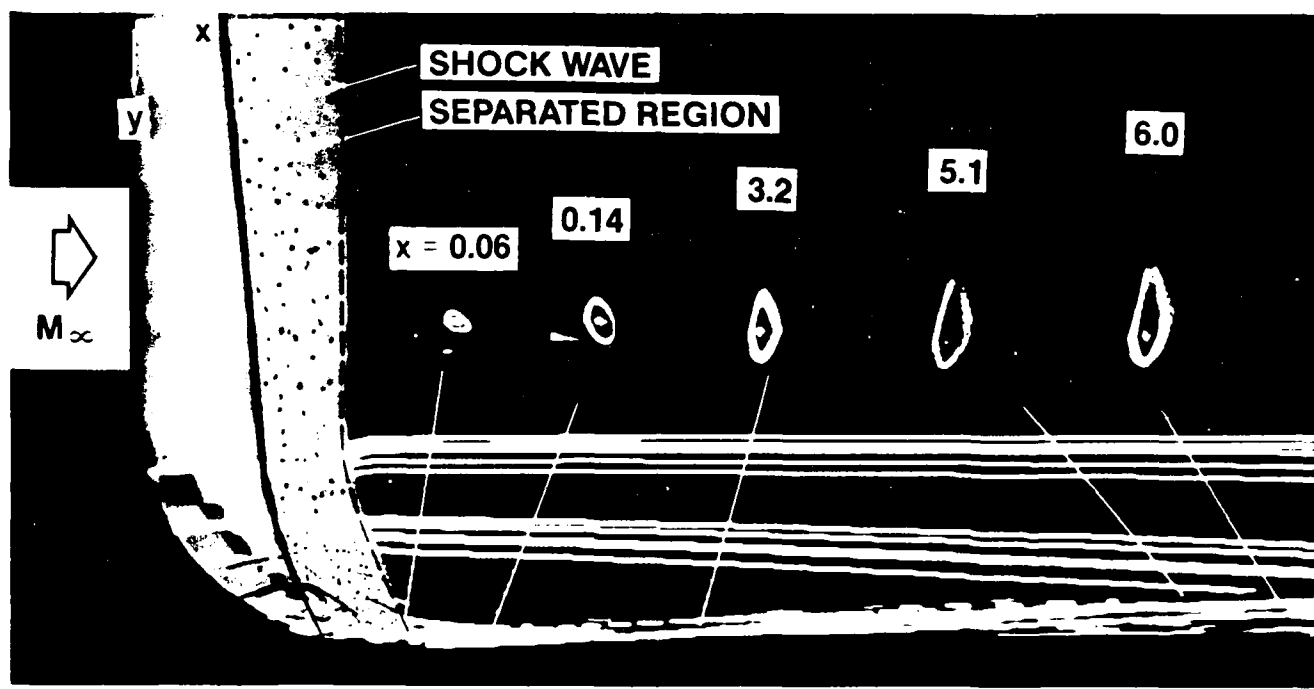


Fig. 12. Farfield view and vorticity contours of the ONERA wing.

the path of the integral. The larger value corresponds to the the smaller integral path surrounding the tip vortex. The smaller value includes the effect of wake vortex sheet.

Effect of Tip Planform

To study the influence of the tip geometry planform on the tip-vortex formation, the ONERA wing of Fig. 2c was modified to reshape the planform in the tip region, keeping the rest of the geometry the same. The planform and the surface grid for this modified wing is shown in Fig. 2d. This modified wing geometry has an unswept leading edge and looks more like a rectangular wing except the tip region retains the original ONERA wing taper. The free stream flow conditions are identical to the preceeding case. From the steady state results for this wing, the lift, drag, and the pitching-moment coefficients for this wing are $C_L = 0.332$, $C_D = 0.0796$, and $C_M = -0.018$. The significant changes here are the larger force coefficients and the stabilizing pitching moment, in contrast to the slightly destabilizing value for the ONERA wing.

For this case, the shock wave and the resulting shock-induced separation are stronger than for the ONERA wing, and the flow topology is different. Another important difference is the structure of tip vortex. Figure 13 shows a view of the tip vortex for this wing. The formation of a the tip vortex, which involves braiding of fluid particle paths, is delayed toward the trailing edge and the near wake region as seen in Fig. 13; also, the vortex appears more diffuse with a larger core. The nondimensional tip vortex strength determined from integrating the velocity vector around a closed path surrounding the tip vortex yields a value of 0.17 when the path of integral includes the vortex sheet of the wake and a value of 0.21 for the path excluding most of the wake vortex sheet.

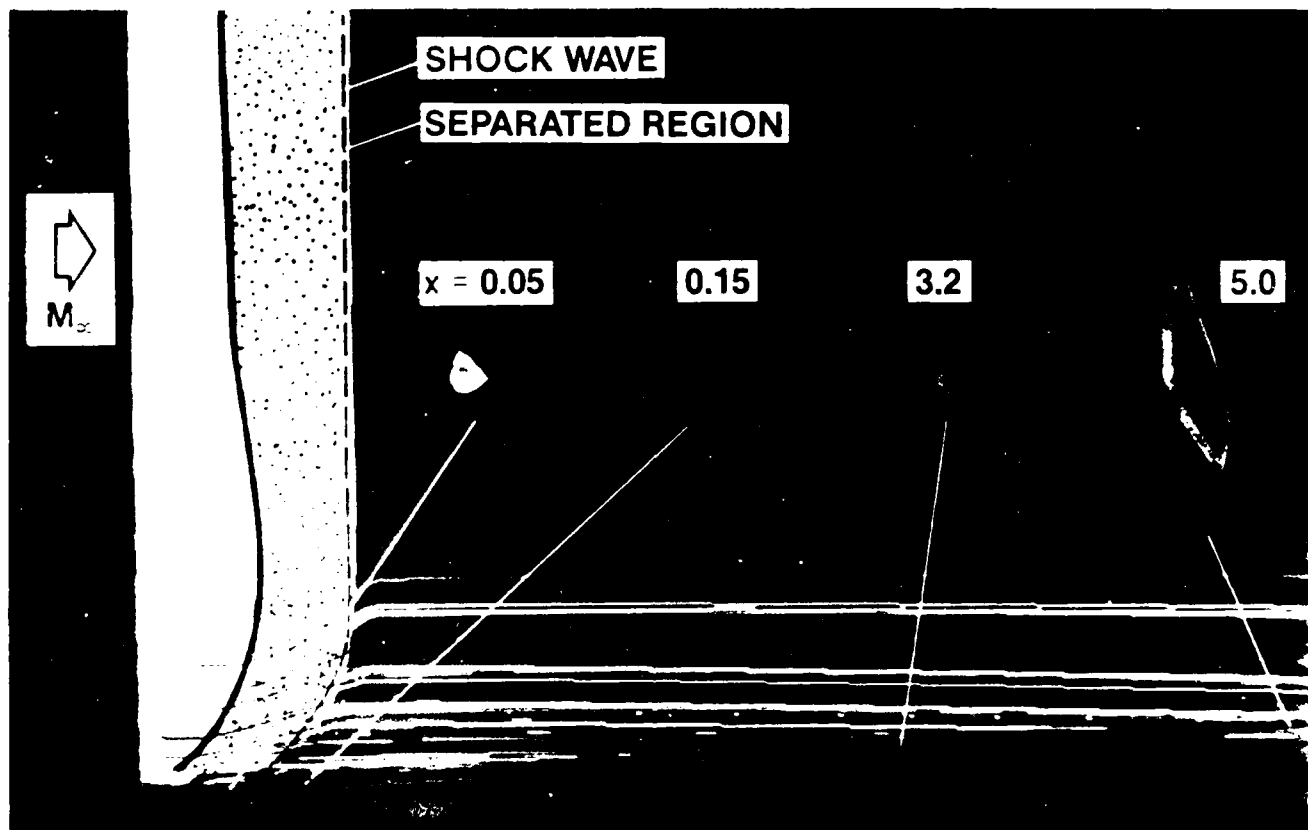


Fig. 13. Farfield view and vorticity contours for the modified ONERA wing $M_\infty = 0.85$, $\alpha = 5^\circ$, and $Re = 2.5 \times 10^6$.

Conclusions

A multi-block zonal algorithm is used for solving the Euler and the Navier-Stokes equations to simulate numerically the formation and roll-up of tip vortices of wings in subsonic and transonic flows. In all, four different wing geometries have been used as test cases. The influence of the tip-planform, the tip-cap shape, and the free-stream Mach number on the formation process has been studied. The numerical results presented here required about 5 - 12 hours of CPU time on the Cray-XMP supercomputer for each steady state solution, depending on the grid size used.

Comparison of the numerical results with the limited available experimental data for both the subsonic and the transonic conditions showed good agreement for the surface pressures, except in the immediate vicinity of the tip and in the shock-induced separated region. The disagreement of surface pressures in the separated region is representative of the current state of the art for predicting transonic shock-induced boundary-layer separation. The subsonic calculations reproduce the qualitative behavior of the experimental tip vortex formation, including the changes in the tip flow separation and in the vortex lift-off due to rounded tip caps that have been observed experimentally. The use of a bevelled tip-cap to mimic a square tip was found to be an inadequate choice. The square-tip simulations do reproduce the correct locations of the suction peaks associated with primary and secondary vortices, but they fail to produce the correct magnitudes for the suction peaks under the vortex. Change of grid topology from H-H to O-O reproduced the same solution without any improvements. These errors may be due to the thin layer assumption, to the deficiencies of a simple turbulence model, and possibly to inadequate grid resolution. Nevertheless, it has been demonstrated that it is possible to calculate the initial development of the tip vortex with out *ad hoc* modeling. The limited study of the tip-cap effect on the flow field near the tip region, presented here, suggests that the tip shape is an important ingredient of the problem.

As expected, the formation of the tip vortex involves braiding of the fluid particle paths in the tip region from both the upper and lower surfaces of the wing. For a lifting

wing the particles from underneath the wing (high-pressure side) cross over the tip face to the upper surface (low-pressure side) and modify the flow field in the tip region by the three-dimensional tip-relief action. The tip vortex first lifts off the surface and then rolls up and moves inboard of the tip, staying distinctly above the wake vortex sheet. Both tip-cap modification and the tip-planform change influenced the gross lift of the wing and hence of the tip vortex strength. The swept-tip planform had a weaker shock wave, but it also produced a more tightly wound (smaller core) vortex compared to the unswept-tip.

In summary, the results presented here demonstrate that, although there is still room for improvement, realistic and meaningful three-dimensional calculations of viscous flows over wings and their associated tip vortex formation are now feasible. This computational fluid dynamics capability provides a new tool for analyzing and improving the aerodynamic characteristics of wings and rotor blades.

Part II

CALCULATION OF HOVERING ROTOR FLOWFIELDS

Part II

CALCULATION OF HOVERING ROTOR FLOWFIELDS

Introduction

The need to accurately calculate the flowfield of a helicopter rotor in both hover and forward flight is of great practical importance. Unlike the flowfield of a fixed wing, the flowfield of a helicopter rotor is generally more complex to analyze because it provides some of the most complex challenges to be found in the field of applied aerodynamics. This complexity stems from several peculiar problems that are unique to the helicopter rotor, viz., a radially increasing blade speed that is responsible for a high concentration of bound circulation over the outer portion of the blade resulting in a strong trailed vortex, a spiralling wake vortex sheet remaining initially close to the rotor causing strong blade-vortex interactions, a high centrifugal force field in which the blades operate, a relatively large steady state out-of-plane displacement of the rotor blades and aeroelastic response of the rotor itself, and finally, mutual interaction of flowfields of main rotor, tail rotor and the fuselage. These flowfields are often characterized by transonic conditions and associated shock waves which makes the flow more susceptible to three dimensionality and unsteadiness.

The operating characteristics of such rotory wing vehicles are strongly influenced by the the vortex wake. The interaction of this wake with the following blades is a potential source of noise and vibration at low and moderate flight speeds. Accurate prediction of the vortical wake is probably the most important, most studied and the most difficult aspect of helicopter flowfield. Current methods of analysis of the wake range in complexity from relatively simple momentum-theory applications to free wake lifting surface methods. In between these extremes, there are a variety of so-called prescribed-wake models, which generally rely on some degree of empiricism to determine the position of the wake vortices; then the Biot-Savart law is used to calculate the induced velocity field due to these vortices at the plane of the rotor blades. Although such models

are widely used in current prediction techniques, they suffer from the limitation that the empirical determination of the wake shape ignores some of the important details of the flowfield such as the mutual interaction between various vortex elements. Further, they are unreliable for unusual blade planforms and/or twist distributions which are often the case with modern helicopter blade shapes.

The current thrust in calculating the rotor flowfield more accurately, including the wake effects, is pushing the use of state-of-art computational fluid dynamics (CFD) codes to shed more light on the understanding of this problem. Finite difference codes for nonlinear compressible potential equations²⁵⁻³⁰ and the Euler equations³¹⁻³⁸ have been used to calculate the rotor flowfields. Initially developed methods using the potential flow and the Euler formulations were primarily limited to calculating nonlifting rotor flows because of the inherent limitation of not being able to model the vortex wake with these equations, although the Euler formulation has in it the necessary physics to model vorticity transport correctly. These equations basically lack the physical mechanism needed to generate the vortex wake. However, in conjunction with wake models, such as CAMRAD³⁹ and HOVER,⁴⁰ both potential flow and Euler codes have been used extensively to calculate the lifting rotor flowfields. The standard experimental data that is used in validating most of these codes has been the two-bladed rotor data of Caradonna and Tung.⁴¹ An excellent review of some of the currently available inviscid finite-difference numerical methods has been recently presented by Caradonna and Tung.⁴²

As mentioned above, tip vortices are an important part of the helicopter rotor flow field. These vortices, which are generated at the tips of the rotating blades, along with the helical wake vortex sheet have tremendous influence on the operating characteristics of the rotor. Some of the common practical problems caused by such concentrated trailing vortices are the rotor vibration due to unsteady lift fluctuation, increased induced drag and the annoying 'blade-slap', an impulsive noise characteristic are a few to name. Many studies have been made to date to understand and reduce the influence of tip vortices

by means of modifications to the tip geometry of the rotating blades. Various analytical and numerical studies conducted are basically inviscid in nature and therefore preclude the mechanics of the physics necessary to model correctly the formation of the tip vortex which involves the the complex three-dimensional viscous flowfield in the tip region. The thin layer Navier-Stokes simulations of tip-flows have been attempted only recently after bigger and faster supercomputers became available. The studies of Mansour¹ and Srinivasan et al.²⁴ show limited success in simulating the complex tip flows. Simulation of the complete vortex wake now appears possible with proper Navier-Stokes algorithm in conjunction with patched and/or zonal grid topology to discretize the flowfield. Understanding the mechanism of the formation process of the tip vortex and its subsequent roll-up would provide a proper insight to modify these tip flows and alleviate some of the problems caused by them. The ability to preserve the concentrated vortices in the finite difference grid without numerical diffusion⁹ has been the biggest set back until now for much progress in this area. Even the most advanced computational techniques, that use spatial central differencing, lack proper mechanism to preserve concentrated tip vortices and convect them in the flowfield without numerical diffusion. However, the recently developed upwind schemes in conjunction with a proper grid choice appear very promising to preserve and convect concentrated vortices. Alternatively, if the properly captured tip vortex is analytically represented, then prescribed vortex methods⁴³⁻⁴⁴ could be applied to calculate the vortex wake development for several rotations of the blade. These methods have demonstrated the ability to preserve and convect concentrated vortices even in very coarse grid regions without significant numerical diffusion.

The use of Navier-Stokes codes to model the rotor flowfields have been limited in the past primarily because of the large computer memory and CPU time requirements. In fact, these codes may not be very much more expensive to run than some of the Euler codes, but to have a meaningful flow definition in the tip region and in the wake might make such a procedure very expensive. Recently, Wake and Sankar⁴⁵ have presented some nonlifting and lifting calculations for a rotor in hover using a coarse grid with a poor definition of the tip region. The results for surface pressure are in fair agreement

with experimental data. The lifting calculations used a correction to the geometric angle of attack of the blade obtained from the lifting surface code of Ref. 40. In the present study, using a good definition of the tip region, thin-layer Navier-Stokes equations are solved for the flowfield of a rectangular blade in hover with a view to capture the tip vortex also. Both nonlifting and lifting cases have been calculated with subcritical and supercritical tip Mach numbers. Surface pressure distributions and tip flow data are presented and compared with experimental data. Alternate methods of calculating the hover flowfield in a non-hover mode (like an isolated fixed blade), keeping the circulation distribution the same as that of a hovering blade, are explored and the results for these are compared with the hover results. Governing equations and numerical method are presented in the next section followed by results and concluding remarks.

Governing Equations and Numerical Scheme

The governing partial differential equations are the unsteady, thin-layer Navier-Stokes equations given by Eqs. (1-4). For generality, these equations are transformed from the Cartesian reference frame to the arbitrary curvilinear space (ξ, η, ζ, τ) while retaining strong conservation law-form to capture shock waves. These equations along with the equation of state for a perfect gas given by Eq. (5) describe the complete flowfield.

In these above equations, u , v , and w are the Cartesian components of the velocity in the inertial coordinate system (x, y, z, t) . In the present formulation Eqs. (1-5) are solved in the inertial frame of reference. The inertial coordinates $\vec{X} = (x, y, z, t)$ are related to the blade fixed coordinates $\vec{X}_b = (\tilde{x}, \tilde{y}, \tilde{z}, \tilde{t})$ through the relation given by

$$\begin{aligned} \vec{X}(x, y, z) &= \mathbf{R}(t)\vec{X}_b(\tilde{x}, \tilde{y}, \tilde{z}) \\ t &= \tilde{t} \end{aligned} \quad (7)$$

where $\mathbf{R}(t)$ is the rotational matrix⁴⁶ given by

$$\mathbf{R}(t) = \begin{bmatrix} \cos \Omega \tilde{t} & -\sin \Omega \tilde{t} & 0 \\ \sin \Omega \tilde{t} & \cos \Omega \tilde{t} & 0 \\ 0 & 0 & 1 \end{bmatrix} \quad (8)$$

Here Ω is the reduced frequency of the rotor and Ωt represents the azimuth sweep of the rotor blade. In view of this relation, Eq. 8, the metrics in inertial reference frame are related to those in the blade-fixed frame of reference through

$$\begin{aligned}
 \xi_x &= \xi_{\bar{z}} \cos \Omega \bar{t} - \xi_{\bar{y}} \sin \Omega \bar{t} \\
 \xi_y &= \xi_{\bar{z}} \sin \Omega \bar{t} + \xi_{\bar{y}} \cos \Omega \bar{t} \\
 \xi_z &= \xi_{\bar{z}} \\
 \eta_x &= \eta_{\bar{z}} \cos \Omega \bar{t} - \eta_{\bar{y}} \sin \Omega \bar{t} \\
 \eta_y &= \eta_{\bar{z}} \sin \Omega \bar{t} + \eta_{\bar{y}} \cos \Omega \bar{t} \\
 \eta_z &= \eta_{\bar{z}} \\
 \zeta_x &= \zeta_{\bar{z}} \cos \Omega \bar{t} - \zeta_{\bar{y}} \sin \Omega \bar{t} \\
 \zeta_y &= \zeta_{\bar{z}} \sin \Omega \bar{t} + \zeta_{\bar{y}} \cos \Omega \bar{t} \\
 \zeta_z &= \zeta_{\bar{z}} \\
 \xi_t &= \Omega \bar{y} \xi_{\bar{z}} - \Omega \bar{x} \xi_{\bar{y}} \\
 \eta_t &= \Omega \bar{y} \eta_{\bar{z}} - \Omega \bar{x} \eta_{\bar{y}} \\
 \zeta_t &= \Omega \bar{y} \zeta_{\bar{z}} - \Omega \bar{x} \zeta_{\bar{y}}
 \end{aligned} \tag{9}$$

The equations set, Eq. 1, is solved using an implicit, approximately-factored numerical scheme that uses spatial central differencing in the η and ζ directions and upwind differencing in the ξ direction developed by Ying et al.⁴⁷ The flux vector \hat{F} has been split in to \hat{F}^+ and \hat{F}^- according to its eigenvalues. Artificial dissipation terms (second- and fourth-order) have been added in the central differencing directions for stability reasons.³ The factored operators can be solved by sweeping in the ξ direction and inverting tridiagonal matrices with 5×5 blocks for the other two directions. Currently, significant part of the computational time is taken to form the plus and minus Jacobian matrices for the flux vector \hat{F} with this numerical scheme. The numerical code is vectorized for the Cray-2 supercomputer.

A body conforming finite-difference grid has been used for the rectangular blade

having a rounded-tip cap and consists of warped spherical O-O grid topology. The flowfield grid is numerically generated using the three-dimensional hyperbolic grid solver of Steger and Chaussee⁴⁸ with proper clustering in the leading and trailing edge regions and in the tip region. The grid is nearly orthogonal at the surface and the spacing in the normal direction at the surface is chosen to be 0.00006 of the chord. All the computations were done with one grid topology having 155 points in the periodic direction around the airfoil, and 66 points each in the spanwise and normal directions, for a total of about 700,000 grid points. The grid boundary is chosen to be at 10 chords in all directions.

The boundary conditions consist of surface boundary conditions and farfield boundary conditions and are applied explicitly. For the nonrotating blade the noslip condition is enforced at the wall by setting U , V and W to be zero and ξ_t , η_t and ζ_t are zero as the grid is stationary. For the rotating blade, however, U , V and W are still set to zero but ξ_t , η_t and ζ_t are nonzero as the blade (and the grid attached to it) is moving in azimuth. Also, at the wall the density is determined by assuming adiabatic wall condition. The pressure along the body surface is calculated from the normal momentum relation (see for example Ref. 25). Having known the density and pressure, the total energy is determined from the equation of state.

At the farfield boundary the flow quantities are either fixed or extrapolated from the interior depending on whether the flow is subsonic or supersonic and if it is of inflow- or outflow-type at the boundary. The characteristic velocities of the Euler equations determine the number of flow properties to be specified to control the reflections of waves from the boundaries. For subsonic-inflow boundary, four quantities must be specified. Thus density is extrapolated while the velocities and the total energy are specified by the free stream values. For supersonic-inflow, all flow quantities are specified. At subsonic-outflow boundaries, only one quantity is specified, viz., pressure is fixed. For supersonic-outflow condition all flow quantities are extrapolated from the interior. At the plane containing the blade root $\partial Q/\partial y = 0$ is imposed.

Results and Discussion

Both time accurate and time asymptotic (steady state) calculations are performed in this study for an aspect ratio 6 rectangular blade having no twist or taper. The blade, which has a round tip-cap (body of revolution), is made up of NACA0012 airfoil section. The rotating blade calculations presented here have been chosen to correspond to the experimental test conditions of a two-bladed hovering rotor of Caradonna and Tung.⁴¹ At the Reynolds number corresponding to the tip speeds in this test, the boundary layer can be assumed to be turbulent over the entire blade and Baldwin and Lomax algebraic turbulence model¹⁰ is used to calculate the turbulent eddy viscosity. A typical solution, with vectorized code for Cray-2, required about 700-1000 marching steps (approximately 45-60 degrees of azimuth travel) to reach quasi-steady flow conditions with CPU time per time step per grid point of 8.5×10^{-5} sec. Time accurate calculations were run with a maximum value for the time step of $\Delta t = 0.01$, whereas the fixed blade option used variable time step option⁴³ with Δt of 5 to calculate steady state flowfield.

Hovering Blade

As mentioned before, the rotating blade calculations presented here correspond to the two-bladed hover test conditions of Caradonna and Tung.¹⁷ Hover calculations have been done in a time accurate fashion. In practice, a hovering rotor flowfield is quasi-steady in blade-fixed coordinates system. Since the governing equations are being solved in the inertial reference frame in the present approach, the flowfield never reaches steady state in this reference frame. This approach was preferred since it is easily extendable to the forward flight case.

Figure 14 shows the chordwise surface pressure distributions at several radial stations for the nonlifting rotor with tip Mach number $M_{tip} = 0.52$ and a corresponding Reynolds number of 2.32 million. As seen, the calculated results are in excellent agreement with experimental data at all radial stations. Accurate calculation of lifting rotor flowfields is possible only if the induced effects of the wake are properly included in the analysis. At present a number of methods are available to model the effects of the wake of a hovering rotor. All these methods seem to give approximately the same kind of

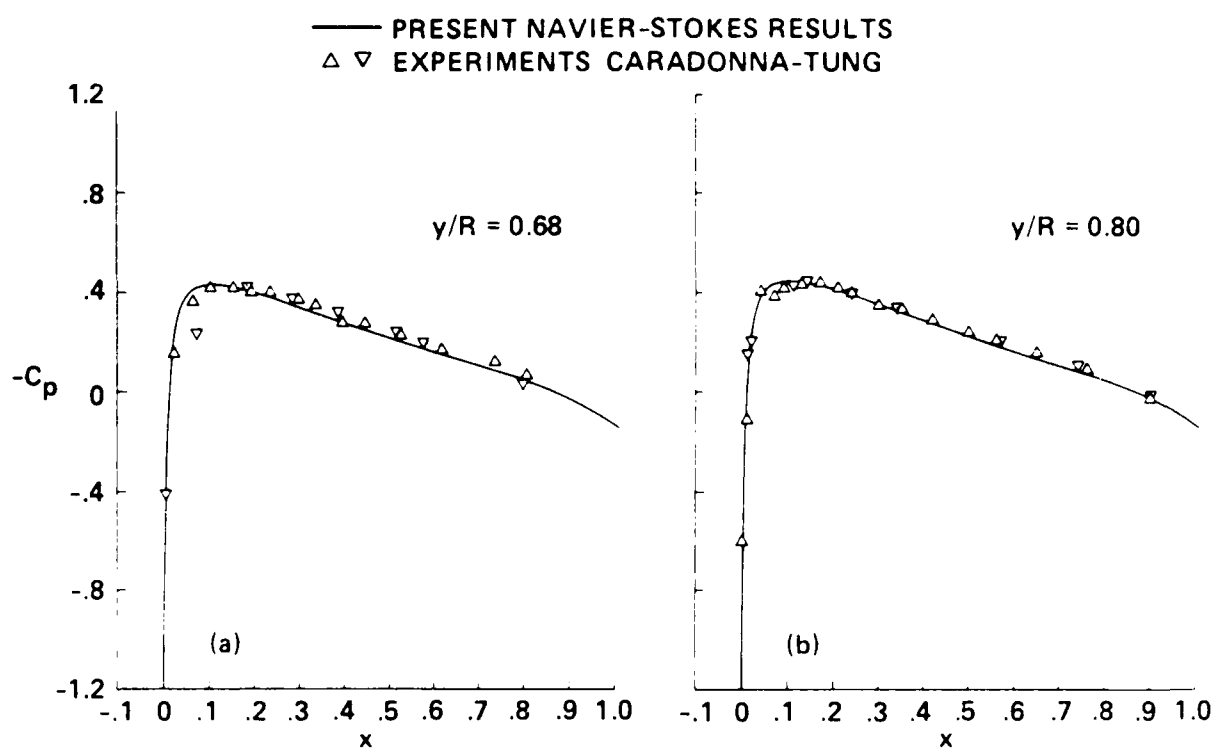


Fig. 14. Surface pressure distributions on a nonlifting rotor in hover;
 $M_{tip} = 0.52$, $Re = 2.32$ million.

results when applied to a particular problem, not dominated by viscous effects, as is shown in the review of Caradonna and Tung.⁴² With this observation, a uniform correction to the angle of attack of the blade has been made in this study based on the estimates of induced downwash for the experimental test rotor configuration given by Agarwal and Deese.³⁵ Figure 15, reproduced from Ref. 35, shows plots of sectional induced velocity estimated from a free-wake analysis program for three speeds of rotor and thrust coefficients of an experimental configuration. Over a section of the blade, approximately from 0.4 to 0.9 radius in this figure, the induced downwash given by the ratio of sectional induced velocity to the local blade speed is nearly constant equal to -3.8 degrees for the entire range of test conditions. In the present calculations this induced downwash is chosen as a representative value and is assumed constant for the entire blade.

The effective pitch of the hovering blade is then the difference of the geometric angle of attack and the induced downwash estimated above. Using this estimate, lifting calculations have been performed for hovering blades set at an effective pitch of 4.2 degrees and having tip Mach numbers of 0.44 and 0.877, respectively. Figures 16 and 17 show the computed results for these cases in the form of surface pressure distributions for representative blade radial stations compared with the experimental data of Caradonna and Tung.⁴¹ The comparison shows very good agreement, at least for the radial stations between 0.6 to 0.95 of radius, for both subcritical and supercritical cases. The agreement progressively deteriorates for radial stations less than 0.6R which probably is expected from the data of Fig. 15. Agarwal and Deese³⁵ have also calculated the same flow using the finite volume Euler formulation and the same induced downwash correction. They also get similar agreement with the experimental data for the subcritical case. However, the shock locations are over estimated for supercritical case in their calculations.

Additional flowfield data for the tip region are presented in Figs. 18-24 for the two lifting cases calculated here. It is well known that the formation of tip vortex involves complex three-dimensional flow separation in the tip region as a necessary condition.

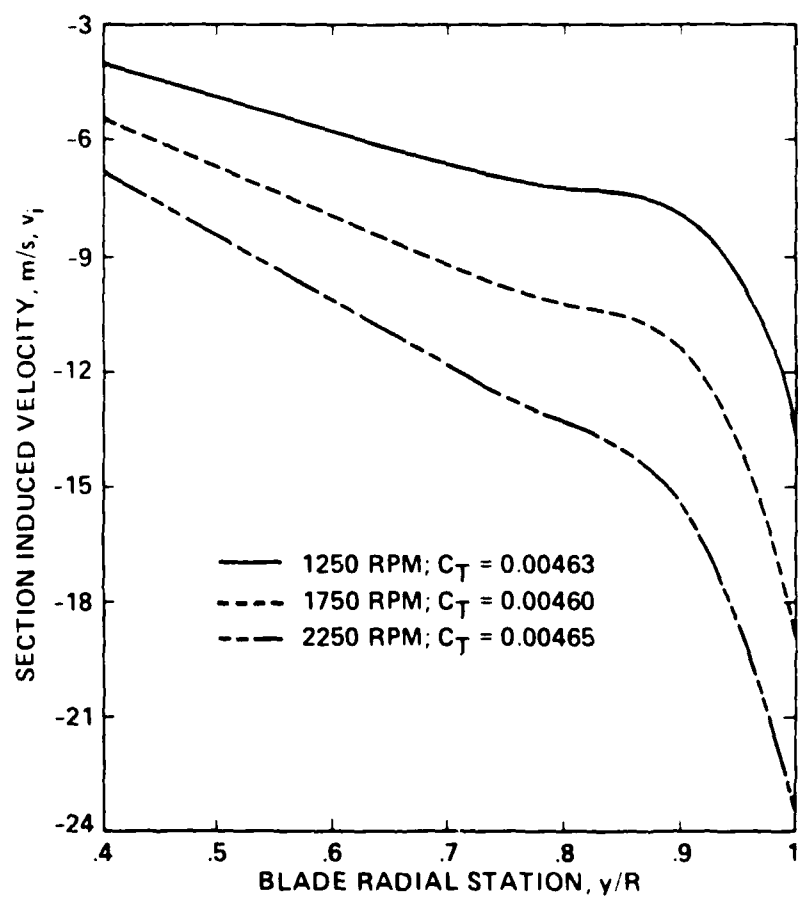


Fig. 15. Wake-induced velocity distribution along the radius of a hovering rotor blade obtained from a Free-Wake Analysis Program. (Figure reproduced from Ref. 11)

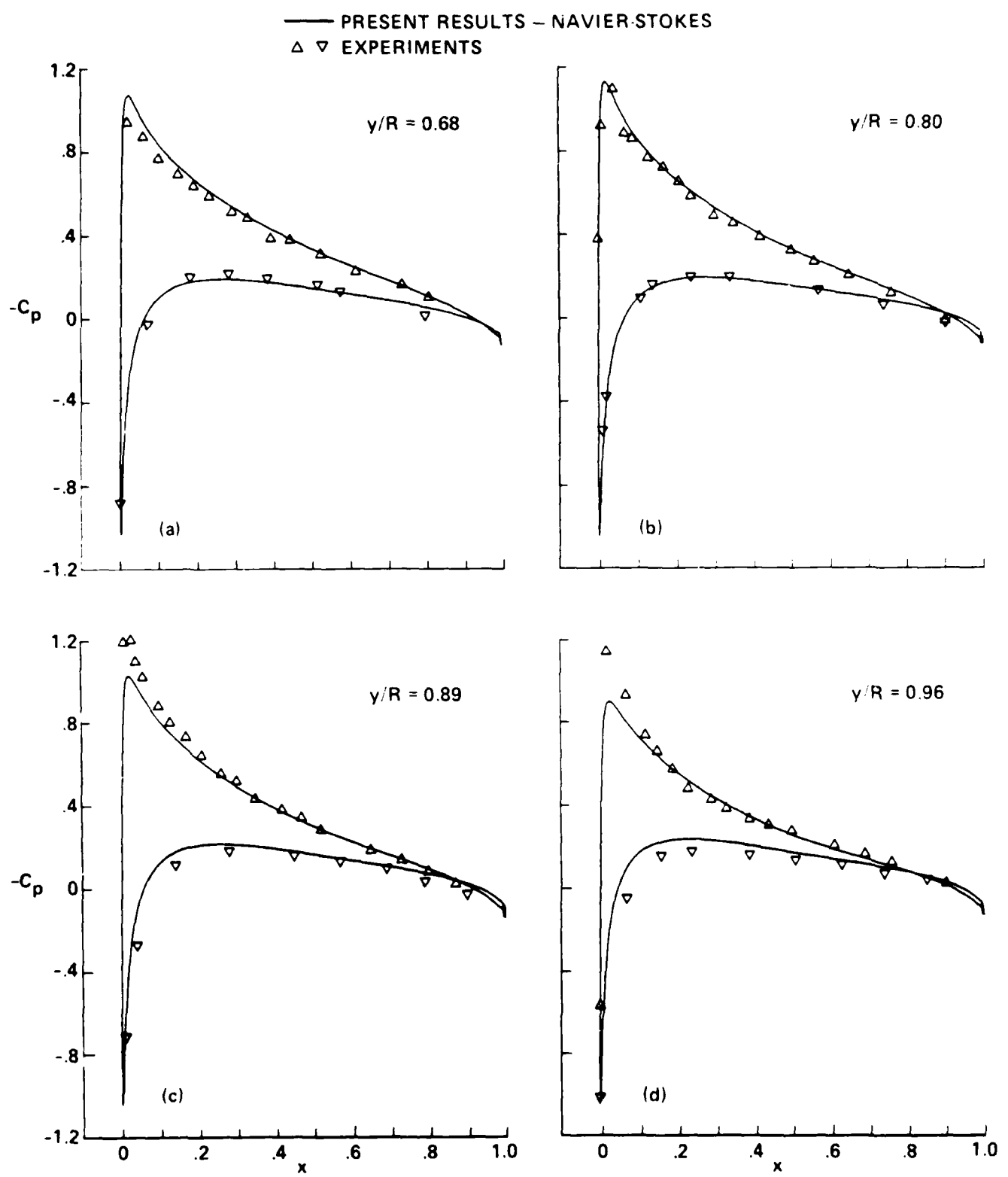


Fig. 16. Surface pressure distributions on a lifting rotor in hover,
 $M_{tip} = 0.44$, Effective pitch = 4.2 deg., $Re = 1.9$ million.

— PRESENT RESULTS - NAVIER-STOKES
 △ ▽ EXPERIMENTS

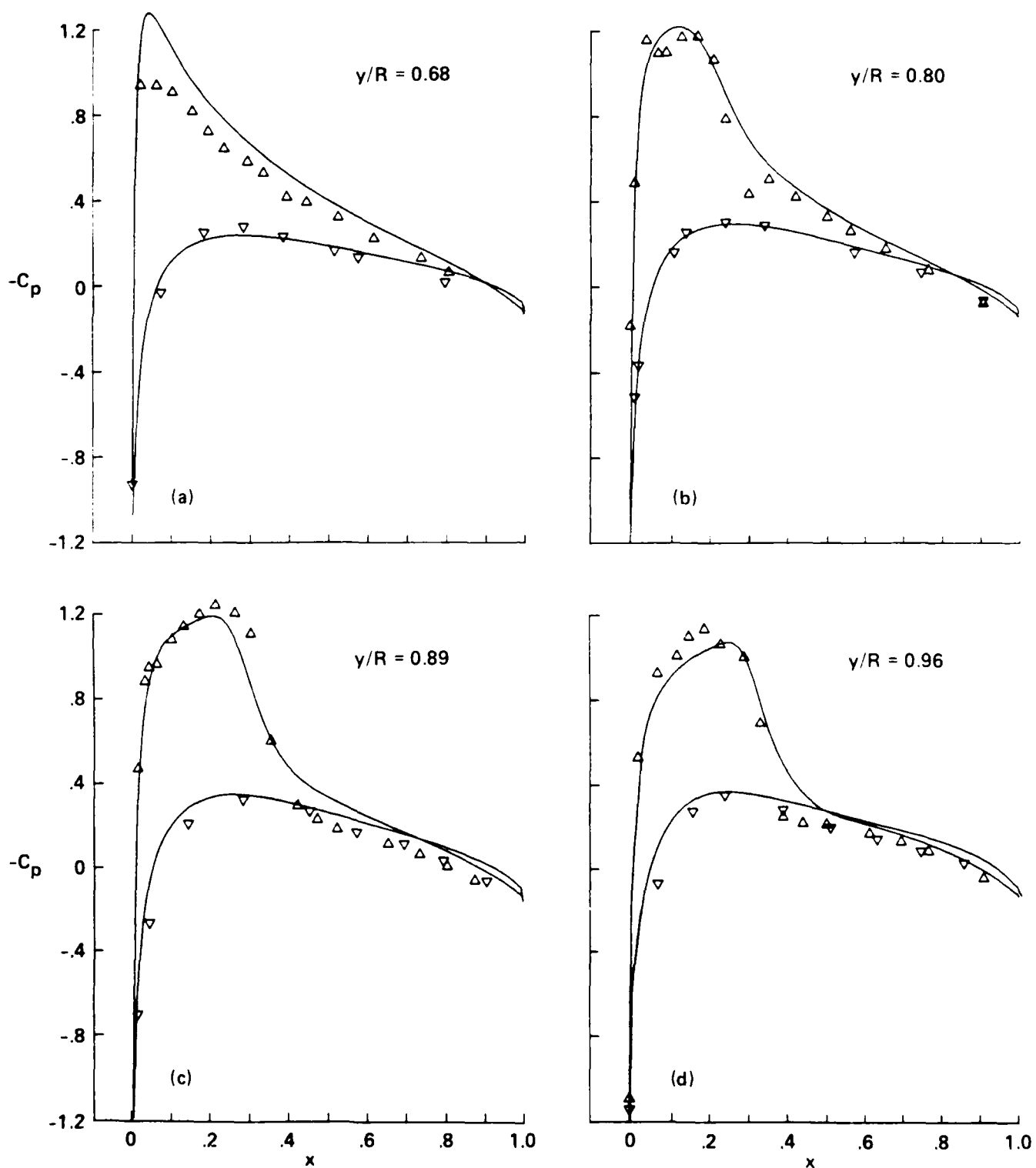
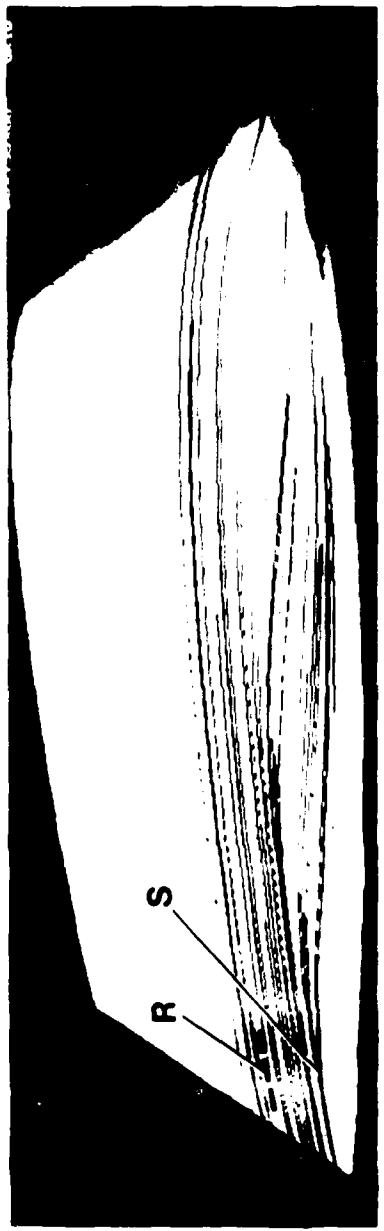


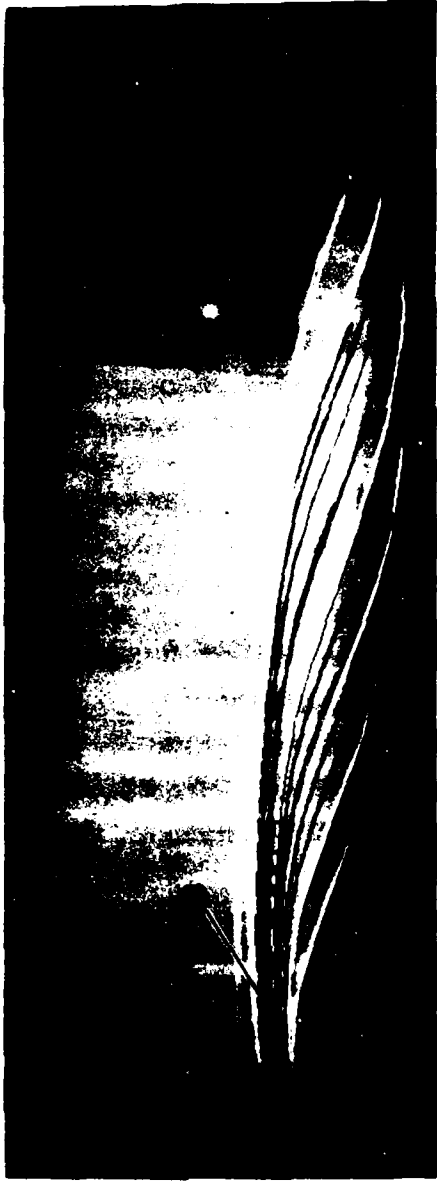
Fig. 17. Surface pressure distributions on a lifting rotor in hover;
 $M_{tip} = 0.877$, Effective pitch = 4.2 deg., $Re = 3.83$ million.

Figure 18a shows a view of the surface particle flow traces in the tip region for the subcritical lifting configuration corresponding to a tip Mach number of $M_{tip} = 0.44$. It is generated by releasing fluid particle tracers at one grid point above the surface and confining the flow to stay in that plane. This view is supposed to mimic the surface oil flow pattern often used in laboratory experiments. The separation and reattachment lines of the flow are marked by the symbols S and R respectively in Fig. 18a. The extent of separation on the upper surface, inboard of tip, is much larger compared to the mild separation seen on the lower surface of the tip region. The braiding of flow particle tracers, released from different locations on the upper and lower surfaces, in the tip region show the formation process of tip vortex in Fig. 19a. In contrast to a nonrotating blade,²⁴ the braiding of particle tracers from upper and lower surfaces is delayed until after the vortex lifts-off from the surface. The initial braiding process is comprised of mostly the particles from the upper surface as is clearly seen in Fig. 19a. The strength of the vortex is determined, as before,²⁴ by the line integral of the velocity vector over a closed path enclosing the vortex. Estimations done at several locations in the downstream wake by this method gave a value of 0.08 to 0.09 depending on the size of the line integral path chosen for the vortex strength. The integrated lift from the blade pressure distributions was found to be 0.19. The vorticity contours shown in Fig. 19a show the size and shape of the tip vortex. As expected, the coarse grid has smeared-off the tightly wound vortex as seen in this figure.

Similar results are presented for the lifting hovering rotor blade with $M_{tip} = 0.877$ in Figs. 20-23. The pressure contours of Fig. 20a show the extent of transonic flow and steepening of the shock wave towards the tip region. The surface particle flow pattern of Fig. 21a clearly identify the regions of separation and reattachment. As before, the separation seen on the lower surface in the tip region is milder compared to the extent seen inboard of the upper surface. The formation process of the tip vortex, seen in Fig. 22a, shows the braiding of particle tracers initially consisting mostly from the upper surface before lifting-off the upper surface inboard of the tip. Further braiding of this from the particles from the lower surface occurs in the wake during the roll-up process.



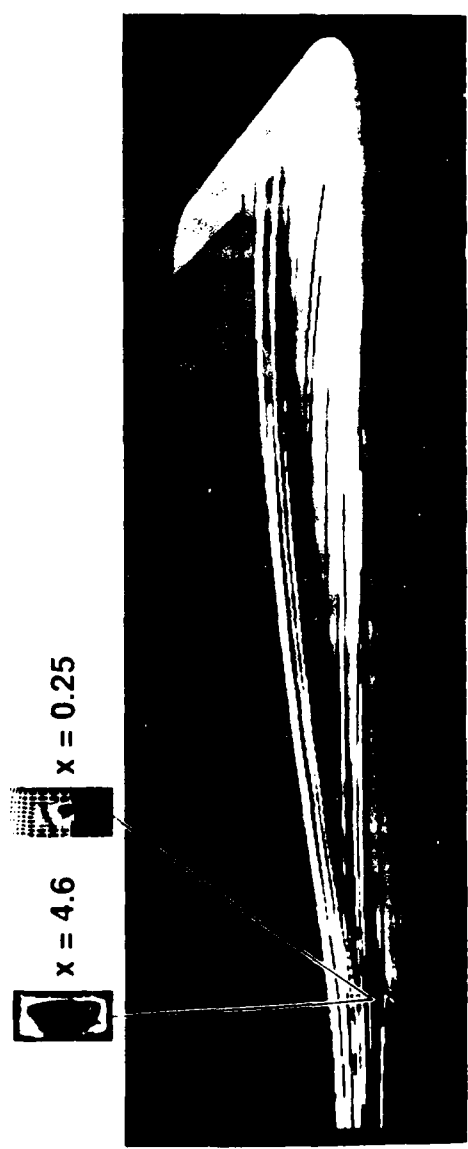
a) ROTATING BLADE



b) FIXED BLADE - $M_{\infty}(y)$

Fig. 18. Surface particle flow traces in the tip region of a lifting rotor blade;

$M_{tip} = 0.44$, $Re = 1.92$ million.



a) ROTATING BLADE



b) FIXED BLADE - M_∞(y)

Fig. 19. View of the tip vortex formation and lift-off from the surface for a lifting rotor blade;
 $M_{tip} = 0.44$, $Re = 1.92$ million.

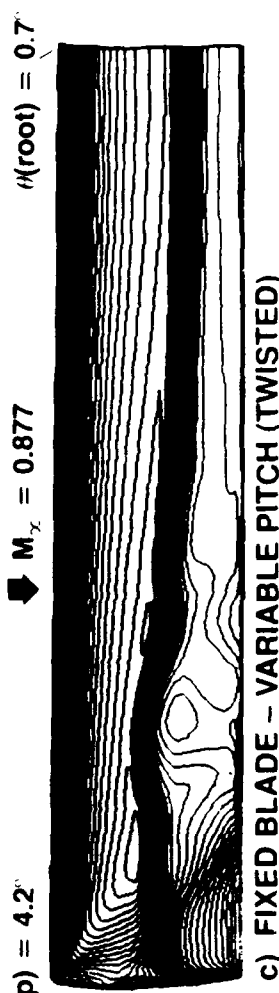
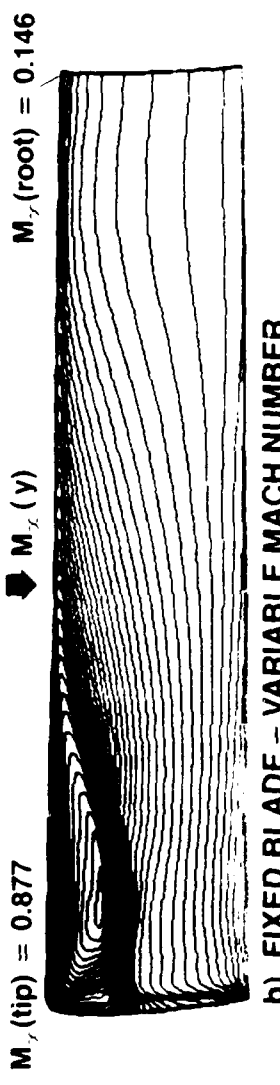
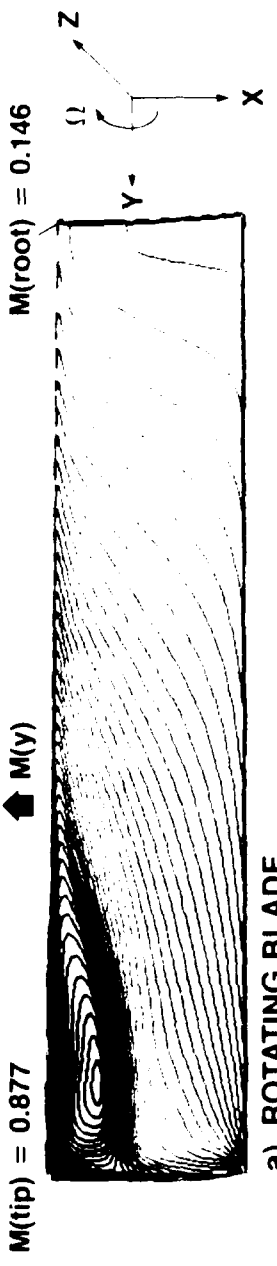


Fig. 20. Surface pressure contours of a lifting blade; $M_{\text{tip}} = 0.877$, $Re = 3.93$ million.



a) ROTATING BLADE



b) FIXED BLADE - $M_{\infty}(y)$



c) FIXED BLADE - $\theta(y)$

Fig. 21. Surface particle flow traces in the tip region of lifting rotor blades;
 $M_{tip} = 0.877$, $Re = 3.93$ million.

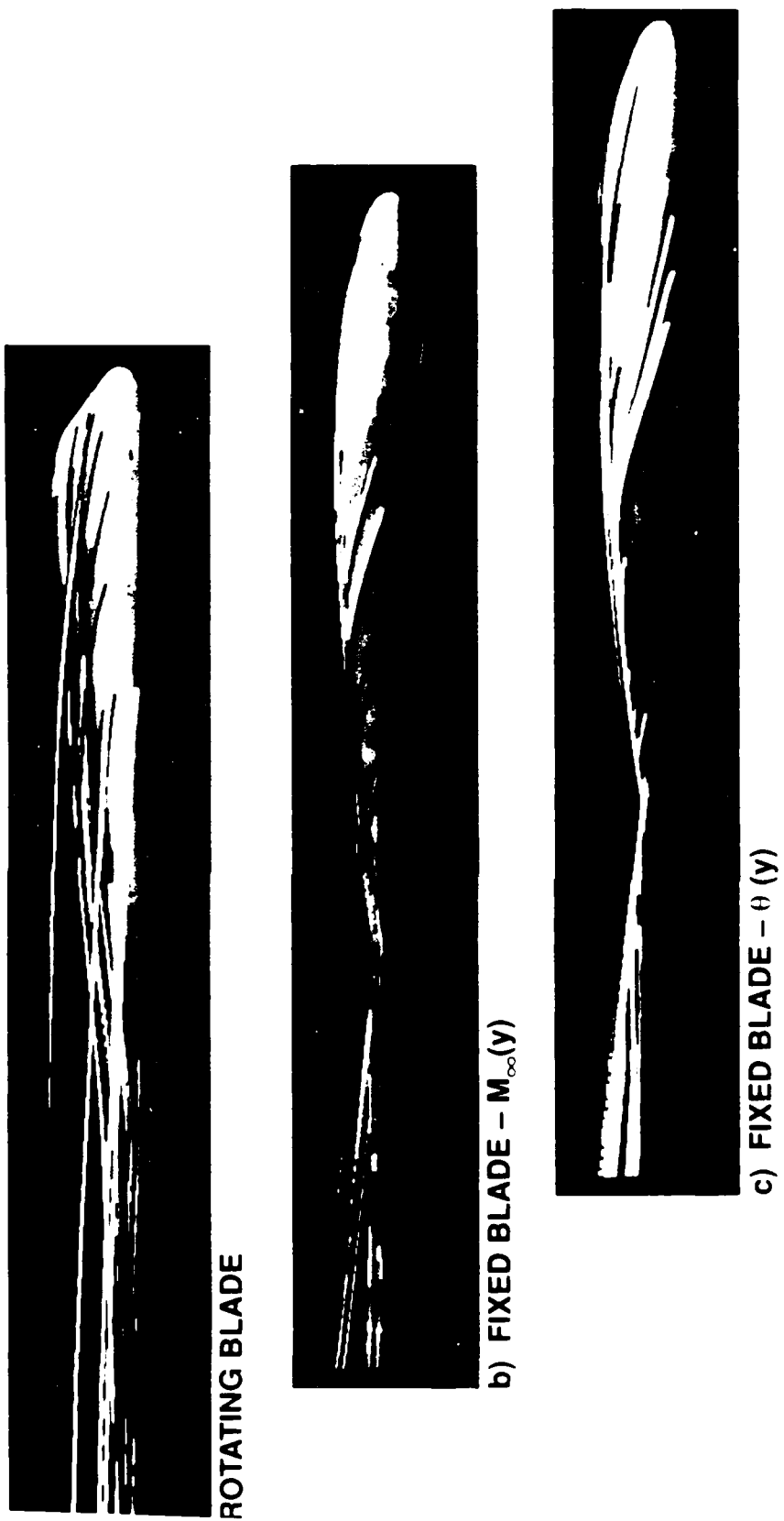


Fig. 22. Near-field view of tip vortex formation and lift-off from the surface of lifting rotor blade; $M_{tip} = 0.877$, $Re = 3.93$ million.

$x = 4.6$ $x = 1.0$ $x = 0.25$



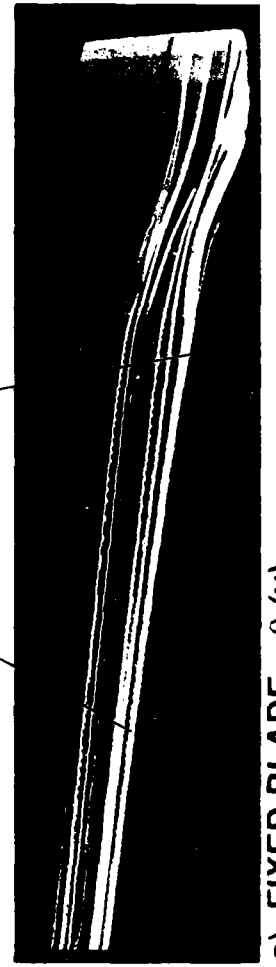
a) ROTATING BLADE

$x = 4.6$ $x = 0.25$



b) FIXED BLADE - $M_{\infty}(y)$

$x = 4.6$ $x = 0.25$



c) FIXED BLADE - $\theta(y)$

Fig. 23. Far-field view of tip vortex showing roll-up in the wake of lifting rotor blade;
 $M_{tip} = 0.877$, $Re = 3.93$ million.

The view looking at the tip, seen in Fig. 22a, clearly shows the lifting-off of the tip vortex from the separated region on the upper surface. A farfield view of this vortex is shown in Fig. 23a. The vorticity contours shown in this figure at different x-locations in the wake suggests approximate shape of the vortex. The strength of this vortex estimated as before gave a value of 0.07-0.08. The integrated value of the lift coefficient for this case is 0.17.

Fixed Blade

The results presented in the above section for the hovering blade were computed in a time accurate manner as mentioned before and these are time consuming and expensive. So this section explores alternate methods to compute the quasi-steady flowfield of the hovering rotor, in particular, as flowfield of a fixed blade with the same circulation distribution as that of the hovering rotor blade with the same tip Mach number. Comparing the circulation distribution for these two modes (fixed and rotating blade), one can immediately come up with two different ways of generating approximately the same circulation distribution on a fixed blade as that of the hovering blade keeping the planform of the blade same by *a*) having the flow Mach number distributed as a function of the radial distance exactly like a hovering blade, keeping every thing else same, and *b*) alternatively keeping the flow Mach number uniform for the entire blade equal to the tip speed and then have a twist distribution along the blade which decreases from the tip to the root of the blade. This means that the fixed blade will have variable twist increasing towards the tip to a value equal to the value of effective pitch of the hovering blade. A third option, that of increasing the chord linearly from the root to the tip, was not explored in this investigation.

With the above reasoning, steady state flowfields were calculated like a fixed isolated blade flowfield with the free stream conditions as discussed above. These calculations used a variable time step option⁴³ to accelerate the convergence rate of the numerical procedure. Figures 24 and 25 show these results in the form of surface pressure distributions compared with the hovering rotor results for both subcritical and supercritical

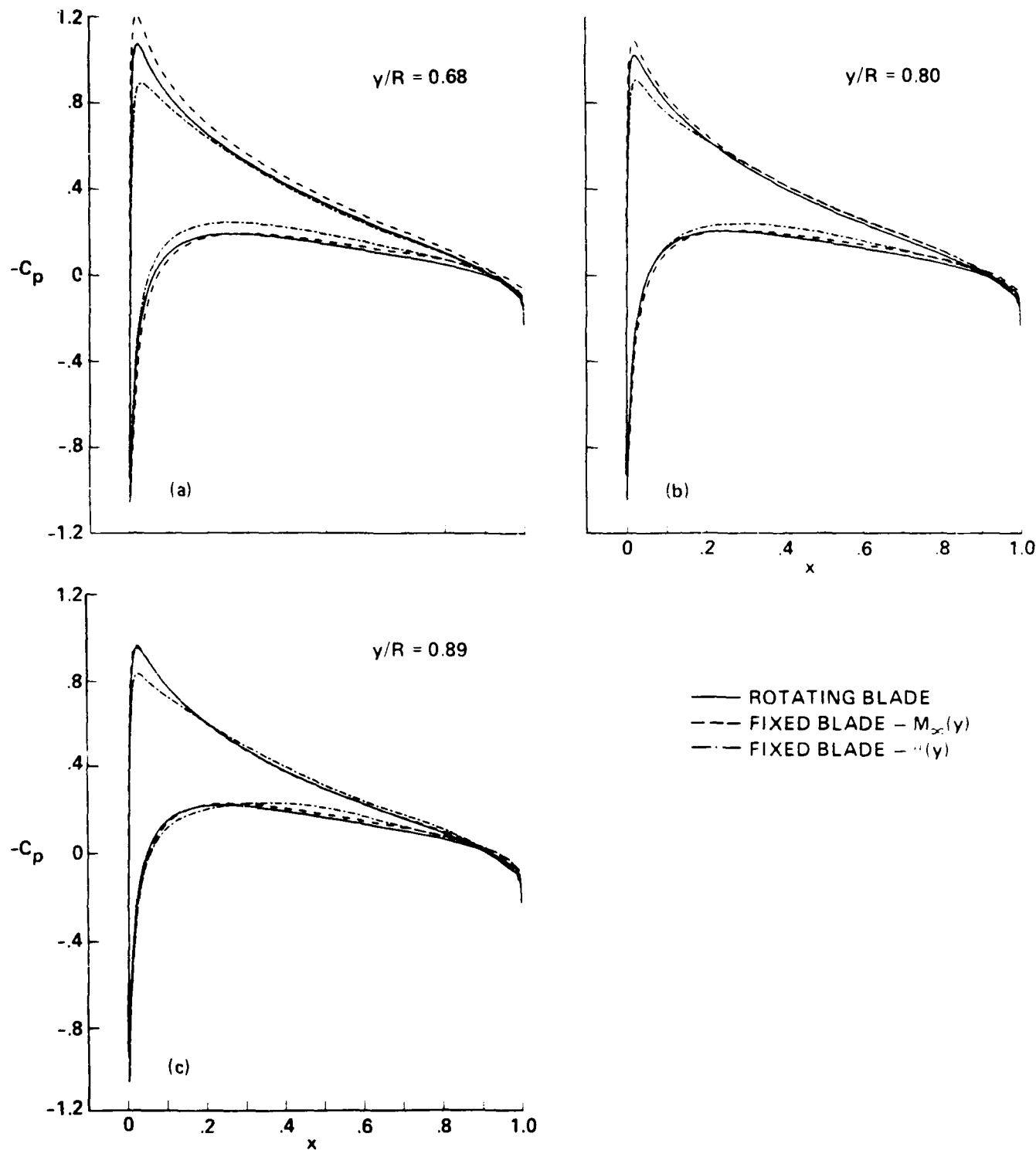


Fig. 24. Comparison of surface pressure distributions for fixed and rotating blades;
 $M_{tip} = 0.44$, $Re = 1.92$ million.

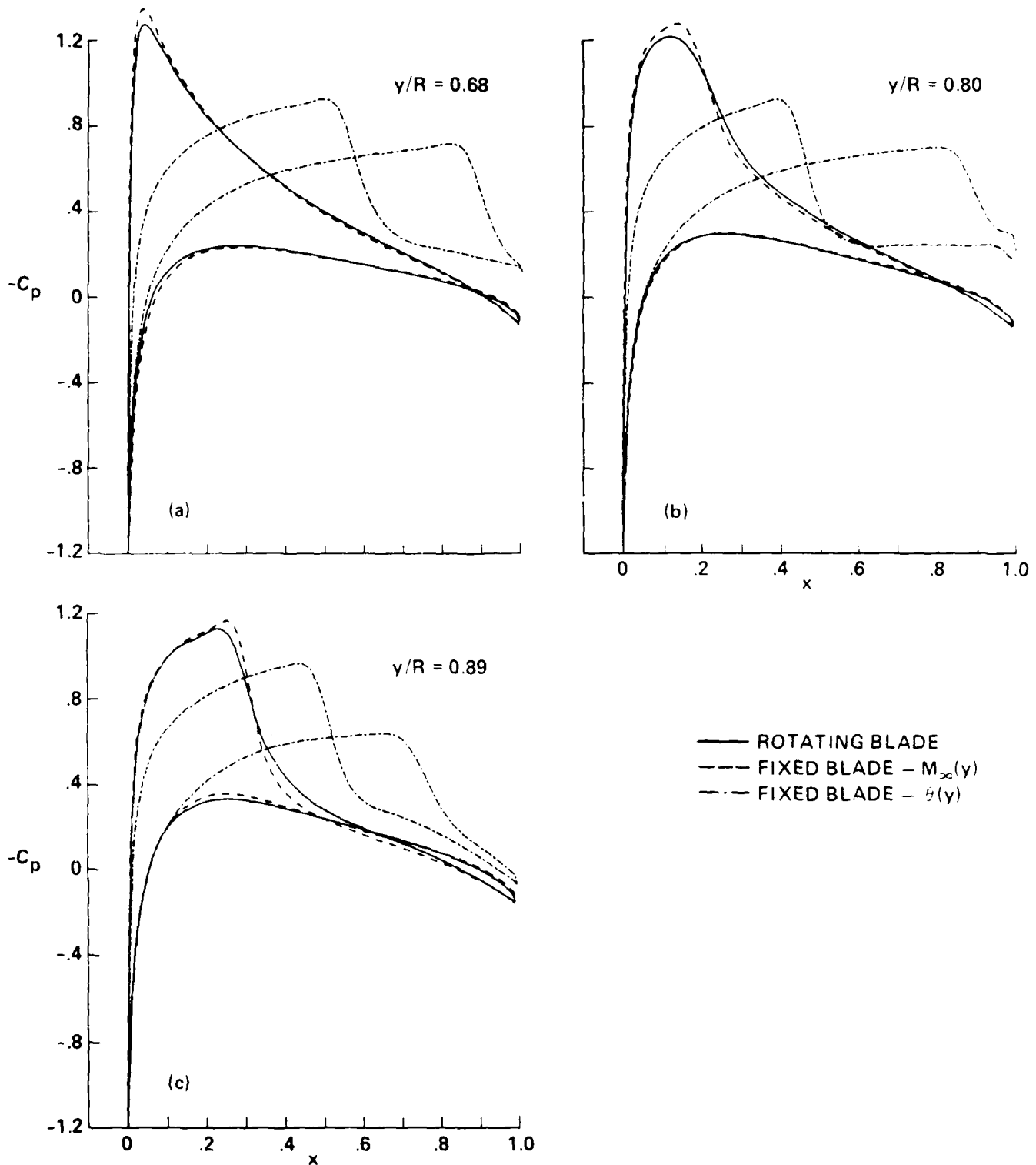


Fig. 25. Comparison of surface pressure distributions for fixed and rotating blades;
 $M_{tip} = 0.877$, $Re = 3.93$ million.

cases. The subcritical results presented in Fig. 24 show surprisingly very good agreement with the hover results for both the options of variable twist and variable Mach number. Considering close agreement of the results even at the radial station near the tip of the blade, the influence of the centrifugal forces present in rotating blade seem to have very little influence in modifying the pressure field in the tip region. There are very small differences in the surface particle flow patterns and the locations of vortex lift-off from the surface for these cases compared to the hovering blade as shown in Figs. 19 and 20. The fixed-blade configurations seem to produce tightly wound vortex even before leaving the blade, but its strength appears to be within 5-10 percent of the hovering blade value.

The supercritical results, presented in Fig. 25, although dominated by the transonic shocks in the tip region show very good agreement of the variable Mach number case with the hover case. The variable twist option does not seem to perform as well in the transonic regime. This is not surprising since high flow Mach number (equal to tip Mach number of rotor) exists all along the span for this non-rotating case. Figures 20b and 20c show the upper surface pressure contour plots for these cases and comparing these with that of hovering blade in Fig. 20a demonstrates the closeness of the variable Mach number fixed-blade case with the hovering case. The variable twist case produces too strong a shock wave along the entire blade with the consequence of producing a totally different flowfield. The close agreement of the flowfield for the cases of Figs. 20a and 7b suggests that even at this supercritical flow condition, the influence of the centrifugal forces appear to have minimal overall effect on the flowfield. However, the surface particle flow pattern seen in Figs. 21a-21c shows differences in the flowfields in the tip region for these cases. The rotating-blade case of Fig. 21a and the fixed-blade case of Fig. 21b although have similar surface pressure distributions, the flow in the tip region near the surface appear different. The difference between the two cases should come from the difference in there force fields, which means that the presence of centrifugal force in the rotating-blade case may have produced a small-scale local separation on the lower surface of the tip in addition to the separation seen on the upper surface of the blade. This separation is clearly is seen in Fig. 21a. The flow in the tip region for the

fixed-blade cases of Figs. 21b and 21c are largely similar even though the flowfield for the case of Fig. 21c is dominated by the strong shock wave and its associated effects. However, the nearfield views of the tip vortices shown in Figs. 22a-22c appear nearly identical, although the lift-off of the tip vortex for hovering blade occurs well inboard of the tip on the upper surface in contrast to the fixed blade cases of Figs. 22b and 22c for which the lift-off appear to occur right in the tip region on the upper surface of the blade. The farfield views of the tip vortices for these cases is shown in Figs. 23a-23c along with vorticity contours insert showing the cross sections of the tip vortices and approximate shapes at various distances from the blade. While the strength of the tip vortex for the variable Mach number case is almost identical to that of the hovering blade case, the variable twist case produced a vortex approximately 2.5 times that of the hovering case. The vortex shapes, determined by the vorticity contour inserts, appear to be same for all cases. It should be emphasised again that these time accurate and steady state calculations were done on the same grid topology to remove the grid dependency from the comparisons.

Conclusions

Unsteady, thin layer Navier-Stokes equations written in rotor coordinates are solved using a flux-split approximately factored, implicit, numerical algorithm to calculate the quasi-steady flowfield of a hovering rotor blade. The test cases chosen correspond to the experimental model hover test conditions of Caradonna and Tung.⁴¹ The numerical results compare very well with the experimental data for both nonlifting and lifting cases. The induced wake effects in the lifting calculations were accounted as a correction to the geometric angle of attack (pitch). Alternate methods are explored to calculate the hovering rotor flowfield as steady state flowfield on fixed isolated blade keeping the same circulation distribution as that of the hovering blade. Of the two options considered, the variable free stream Mach number case gave almost identical results as that of a rotor at both subcritical and supercritical flow conditions. The variable twist option, on the other hand, gave similar results only under subcritical flow conditions; the supercritical flow condition was dominated by strong transonic shocks. Under conditions where the fixed blade flowfield closely agreed with that of hovering blade, the influence of the centrifugal forces of the rotating blade appeared to have minimum influence on the overall flowfield properties. While these conclusions are preliminary and primarily based on the comparison of surface pressures and vortex strength estimates, further quantitative comparison of the vortex structure is needed for a clear understanding of the similarities and differences.

REFERENCES

1. Mansour N. N., "Numerical Simulation of the Tip Vortex Off a Low-Aspect Ratio Wing at Transonic Speed", AIAA Journal, Vol. 23, No. 8, August 1985, pp. 1143-1149.
2. Kaynak, U., Holst, T., Cantwell, B. J. and Sorenson, R. L., "Numerical Simulation of Transonic Separated Flows over Low-Aspect Ratio Wings", Journal of Aircraft, Vol. 24, No. 8, August 1987, pp. 531-539.
3. Pulliam T. H. and Steger J. L., "Implicit Finite-Difference Simulations of Three-Dimensional Compressible Flow", AIAA Journal, Vol. 18, No. 2, February 1980, pp. 159-167.
4. Pulliam, T. H., "Euler and Thin-Layer Navier-Stokes Codes: ARC2D, ARC3D", Notes for the Computational Fluid Dynamics User's Workshop, The University of Tennessee Space Institute, Tullahoma, Tennessee., March 1984.
5. Holst T. L., Gundy K. L., Flores J., Chaderjian N. M., Kaynak U. and Thomas S. D., "Numerical Solution of Transonic Wing Flows Using an Euler/ Navier-Stokes Zonal Approach", Journal of Aircraft, Vol. 24, No. 1, January 1987, pp. 17-24.
6. Flores J., "Convergence Acceleration for a Three-Dimensional Euler/Navier- Stokes Zonal Approach", AIAA Journal, Vol. 24, No. 9, September 1986, pp. 1441-1442.
7. Beam, R. and Warming, R. F., "An Implicit Finite-Difference Algorithm for Hyperbolic Systems in Conservation Law Form", Journal of Computational Physics, Vol. 22, September 1976, pp. 87-110.
8. Pulliam, T. H. and Chaussee, D. S., "A Diagonal Form of an Implicit Approximate-Factorization Algorithm", Journal of Computational Physics, Vol. 39, No. 2, February 1981, pp. 347-363.
9. Srinivasan G. R., Chyu W. J. and Steger J. L., "Computation of Simple Three-Dimensional Wing-Vortex Interaction in Transonic Flow", AIAA Paper 81-1206,

June 1981.

10. Baldwin, B. S. and Lomax, H., "Thin Layer Approximation and Algebraic Model for Separated Turbulent Flows", AIAA Paper 78-257, January 1978.
11. Edwards T. A., "Noniterative Three-Dimensional Grid Generation Using Parabolic Partial Differential Equations", AIAA Paper 85-0485, January 1985.
12. Spivey, W. A. and Moorhouse, G. G., "New Insights into the Design of Swept-Tip Rotor Blades", 26th Annual National Forum of the American Helicopter Society, Washington, D. C., June 1970.
13. Spivey, W. A., "A Study to Investigate the Aerodynamics of Rotor Blade Tip Shapes", Bell Helicopter Company Report No. 299-099-468, January 1970.
14. Steger, J. L. and Chaussee, D. S., "Generation of Body-Fitted Coordinates Using Hyperbolic Partial Differential Equations", SIAM J. Sci. Stat. Comput., Vol.1, No. 4, December 1980, pp. 431-437.
15. Ying, S. X., Steger, J. L., Schiff, L. B. and Baganoff, D., "Numerical Simulation of Unsteady, Viscous, High-Angle-of-Attack Flows Using a Partially Flux-Split Algorithm", AIAA Paper 86-2179, August 1986.
16. Triebstein, H., "Unsteady Pressure Measurements in Rotor Blade Tips with Incidence in Incompressible Flow", European Space Agency Technical Translation, ESA-TT-374-July, 1977.
17. Thomas, J. L., Taylor, S. L. and Anderson, W. K., "Navier-Stokes Computations of Vortical Flows Over Low Aspect Ratio Wings", AIAA Paper 87-0207, January 1987.
18. Thompson, D. H., "A Flow Visualization Study of Tip Vortex Formation", ARL-AERO-NOTE-421, Aerodynamics Note 421, November 1983, Aeronautical Research Laboratories, Melbourne, Australia.

19. Chigier, N. A. and Corsiglia, V. R., "Tip Vortices - Velocity Distributions", NASA TM X-62,087, September 1971.
20. Keener E. R., "Computational-Experimental Pressure Distributions on a Transonic Low-Aspect-Ratio Wing", AIAA Paper 84-2092, August 1984.
21. Hinson, B. L. and Burdges, K. P., "Acquisition and Application of Transonic Wing and Far-Field Test Data for Three-Dimensional Computational Method Evaluation", Vol. Appendix B, Experimental Data, Lockheed Georgia Company, AFOSR-TR-80-0422, 1980.
22. Kaynak, U. and Flores, J., "Advances in the Computation of Transonic Separated Flows Over Finite Wings", AIAA Paper 87-1195, 1987.
23. Desopper, A., "Study of the Unsteady Transonic Flow on Rotor Blades with Different Tip Shapes", VERTICA, Vol. 9, No. 3, 1985, pp. 257-272.
24. Srinivasan, G. R., McCroskey, W. J., Baeder, J. D. and Edwards, T. A., "Numerical Simulation of Tip Vortices of Wings in Subsonic and Transonic Flows", AIAA Paper 86-1095, May 1987; AIAA Journal, Vol. 26, April 1988 (to appear).
25. Caradonna, F. X. and Isom, M. P., "Subsonic and Transonic Potential Flow over Helicopter Rotor Blades", AIAA Journal, Vol. 10, No. 12, December 1972, pp. 1606-1612.
26. Chang, I.-C., "Transonic Flow Analysis for Rotors", NASA TP-2375, 1984.
27. Strawn, R. C. and Caradonna, F. X., "Conservative Full-Potential Model for Unsteady Transonic Rotor Flows", AIAA Journal, Vol. 25, No. 2, February 1987, pp. 193-198.
28. Steinhoff J. and Ramachandran, K. "Free Wake Analysis of Compressible Rotor Flows", AIAA Paper 87-0542, January 1987.

29. Strawn, R. C. and Tung, C., "The Prediction of Transonic Loading on Advancing Helicopter Rotors", Paper presented at the AGARD/FDP Symposium on Applications of Computational Fluid Dynamics in Aeronautics, France, April 1986.
30. Strawn, R. C. and Tung, C., "Prediction of Unsteady Transonic Rotor Loads with a Full-Potential Rotor Code", Proceedings of the 43rd Annual Forum of American Helicopter Society, May 1987, St. Louis, Missouri.
31. Wake, B. E., Sankar, N. L. and Lekoudis, S. G., "Computation of Rotor Blade Flows using the Euler Equations", Journal of Aircraft, Vol. 23, No. 7, July 1986, pp. 582-588.
32. Chen, C. L., McCroskey, W. J. and Ying, S. X., "Euler Solution of Multi-Blade Rotor Flow", Paper No. 2.2, Presented at the 13th European Rotorcraft Forum, Arles, France, September 1987.
33. Roberts, T. W. and Murman, E. M., "Solution Method for a Hovering Helicopter Rotor using the Euler Equations", AIAA Paper 85-0436, January 1985.
34. Kroll, N., "Computations of the Flow Fields of Propellers and Hovering Rotors using Euler Equations", Paper No. 28, 12th European Rotorcraft Forum, Garmisch-Partenkirchen, Federal Republic of Germany, September 1986.
35. Agarwal, R. K. and Deese, J. E., "Euler Calculations for Flowfield of a Helicopter Rotor in Hover", AIAA Paper 86-1782, June 1986.
36. Sankar, N. L. and Tung, C., "Euler Calculations for Rotor Configurations in Unsteady Forward Flight", Proceedings of the 42nd Annual Forum of American Helicopter Society, June 1986, Washington, D. C., pp. 985-995.
37. Chang, I-C. and Tung, C., "Euler Solution of the Transonic Flow for a Helicopter Rotor", AIAA Paper 87-0523, January 1987.
38. Agarwal, R. K. and Deese, J. E., "An Euler Solver for Calculating the Flowfield of

a Helicopter Rotor in Hover and Forward Flight", AIAA Paper 87-1427, June 1987.

39. Johnson, W., "A comprehensive Analytical Model of Rotorcraft Aerodynamics. Part 1, Analysis Development", NASA TM-81182, 1980.

40. Summa, J. M. and Clark, D. R., "A Lifting Surface Method for Hover/Climb Loads", Proceedings of the 35th Annual Forum of the American Helicopter Society, Washington, D. C., May 1979.

41. Caradonna, F. X. and Tung, C., "Experimental and Analytical Studies of a Model Helicopter Rotor in Hover", NASA TM-81232, September 1981.

42. Caradonna, F. X. and Tung, C., "A Review of Current Finite Difference Rotor Flow Codes", Proceedings of the 42nd Annual Forum of the American Helicopter Society, Washington, D. C., June 1986, pp. 967-983.

43. Steinhoff, J. and Suryanarayanan, K., "The Treatment of Vortex Sheets in Compressible Potential Flow", AIAA Paper 83-1881-CP, July 1983.

44. Srinivasan, G. R. and McCroskey, W. J., "Numerical Simulations of Unsteady Airfoil-Vortex Interactions", VERTICA, Vol. 11, No. 1/2, 1987, pp. 3-28.

45. Wake, B. E. and Sankar, L. N., "Solutions of the Navier-Stokes Equations for the Flow About a Rotor Blade", Proceedings of National Specialists' Meeting on Aerodynamics and Aeroacoustics, February 1987, Arlington, Texas.

46. Isom, M. P., "Unsteady Subsonic and Transonic Potential Flow over Helicopter Rotor Blades", NASA CR-2463, October 1974.

47. Ying, S. X., Steger, J. L., Schiff, L. B. and Baganoff, D., "Numerical Simulation of Unsteady, Viscous, High-Angle-Of-Attack Flows Using a Partially Flux-Split Algorithm", AIAA Paper 86-2179, August 1986.

48. Steger, J. L. and Chaussee, D. S., "Generation of Body-Fitted Coordinates Using

Hyperbolic Partial Differential Equations", SIAM J. Sci. Stat. Comput., Vol. 1, No. 4, December 1980, pp. 431-437.

49. Caradonna, F. X., Laub, G. H. and Tung, C., "An Experimental Investigation of the Parallel Blade-Vortex Interaction", Paper No. 4, Tenth European Rotorcraft Forum, August 1984, The Hague, Netherlands.
50. McAlister, K. W. and Tung, C., "Airfoil Interaction with an Impinging Vortex", NASA Tech. Paper 2273, February 1984.
51. Meier, G. E. A. and Timm. R., "Unsteady Vortex Airfoil Interaction", AGARD Symposium on Unsteady Aerodynamics - Fundamentals and Applications to Aircraft Dynamics, Paper No. 16, AGARD CP-386, May 1985.
52. Padakannaya, R., "Experimental Study of Rotor Unsteady Airloads due to Blade-Vortex Interaction", NASA CR - 1907, November 1971.
53. Caradonna, F. X., Tung, C. and Desopper, A., " Finite Difference Modeling of Rotor Flows Including Wake Effects", J. American Helicopter Society, Vol. 29, No. 2, April 1984, pp. 26-33.
54. George, A. R. and Chang, S. B., "Noise Due to Transonic Blade-Vortex Interactions", American Helicopter Society Paper A-83-39-50-D000, May 1983.
55. Srinivasan, G. R., McCroskey, W. J. and Kutler, P., "Numerical Simulation of the Interaction of a Vortex with Stationary Airfoil in Transonic Flow", AIAA Paper 84-0254, January 1984.
56. McCroskey, W. J. and Srinivasan, G. R., "Transonic Interaction of Unsteady Vortical Flows", Third Symposium of Numerical and Physical Aspects of Aerodynamic Flows, Paper No. 5-1, January 1985, Long Beach, California; also NASA TM-86658, December 1984.

57. Srinivasan, G. R., "Computations of Two-Dimensional Airfoil-Vortex Interactions", NASA CR - 3885, May 1985.

58. Wu, J. C., Sankar, N. L. and Hsu, T. M., "Unsteady Aerodynamics of an Airfoil Encountering a Passing Vortex", AIAA Paper 85-0203, January 1985.

59. Jones, H. E., "The Aerodynamic Interaction Between an Airfoil and a Vortex in Transonic Flow", Paper presented at the Workshop on Blade-Vortex Interactions, (Unpublished) October 1984, Moffett Field, California.

60. Caradonna, F. X. and Philippe, J. -J., "The Flow over a Helicopter Blade Tip in the Transonic Regime", Vertical, Vol. 2, No. 1, pp. 43-60, 1978.

61. Pulliam, T. H., Jespersen, D. C. and Childs, R. E., "An Enhanced Version of an Implicit Code for the Euler Equations", AIAA Paper 83-0344, January 1983.

62. Nakahashi, K. and Deiwert, G. S., "A Practical Adaptive-Grid Method for Complex Fluid-Flow Problems", Lecture Notes in Physics, Vol. 218, Springer-Verlag, 1984, pp. 422-426; also NASA TM-85989, 1984.

63. Nakahashi, K. and Deiwert, G. S., "A Self-Adaptive-Grid Method with Application to Airfoil Flow", AIAA Paper 85-1525-CP, July 1985.

64. Buning, P. G. and Steger, J. L., "Solution of the Two-Dimensional Euler Equations with Generalized Coordinate Transformation Using Flux Vector Splitting", AIAA Paper 82-0971, June 1982.

65. Steger, J. L., "Implicit Finite-Difference simulation of Flow about Arbitrary Two-Dimensional Geometries", AIAA Journal, Vol. 16, No. 7, July 1978, pp. 679-686.

66. Caradonna, F. X. and Isom, M. P., "Numerical Calculation of Unsteady Transonic Potential Flow over Helicopter Rotor Blades", AIAA Journal, Vol. 14, No. 4, April 1976, pp. 482-488.

67. Takahashi, R. K. and McAlister, K. W., "Preliminary Measurements of a Wing-Tip Vortex using Laser Velocimetry", (Unpublished Data), Private communication.

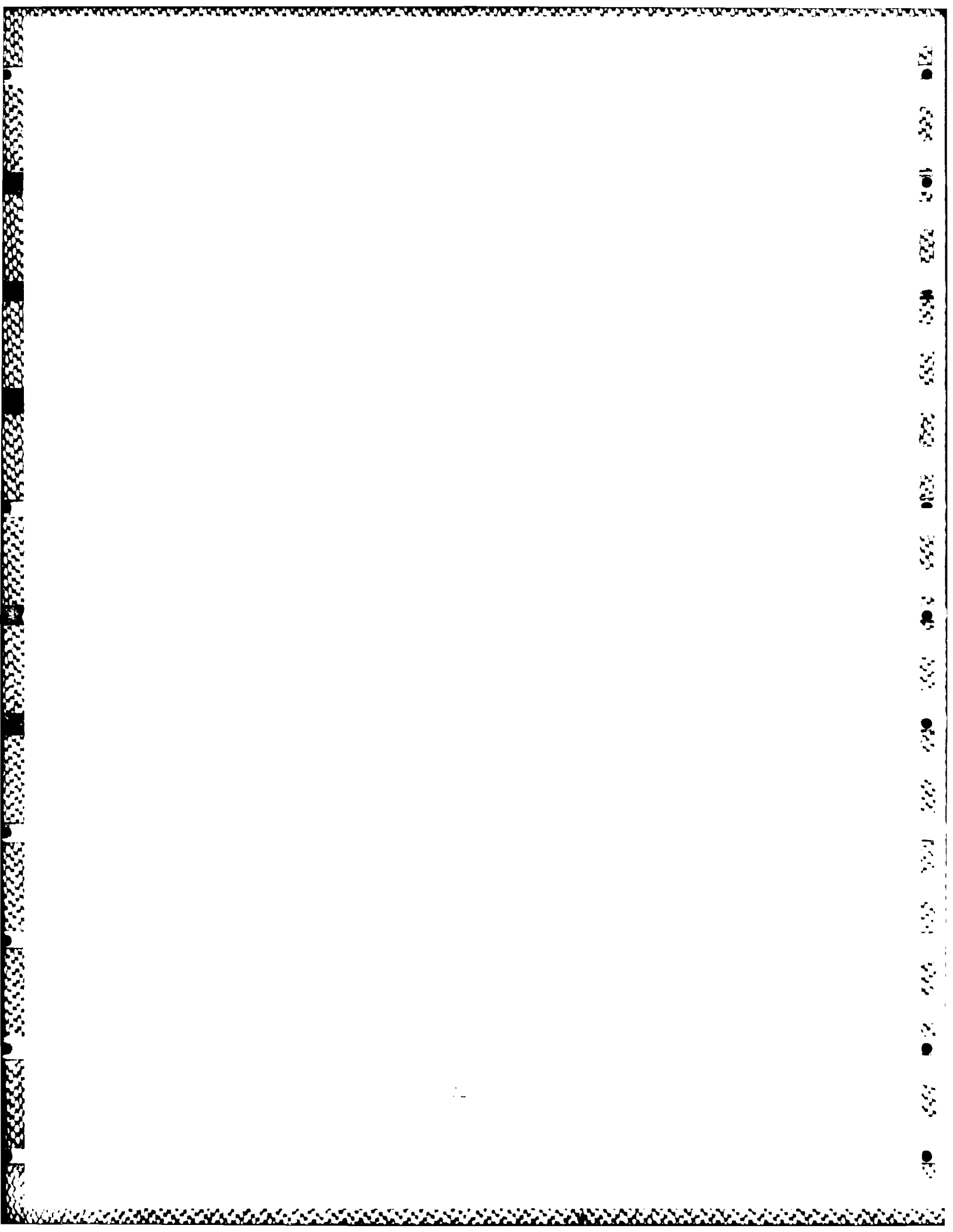
68. Orloff, K. L. and Grant, G. R., "The Application of Laser Doppler Velocimetry to Trailing Vortex Definition and Alleviation", NASA TM X-62,243, February 1973.

69. Tung, C., Private Communicaton.

70. McCroskey, W. J. and Goorjian, P. M., "Interactions of Airfoils with Gusts and Concentrated Vortices in Unsteady Transonic Flow", AIAA Paper 83-1691, July 1983.

Part III

UNSTEADY, TWO-DIMENSIONAL BLADE-VORTEX INTERACTIONS



Aerodynamics of Two-Dimensional Blade-Vortex Interaction

G. R. Srinivasan, W. J. McCroskey, J. D. Baeder

Reprinted from



Volume 24 Number 10 October 1986 Page 1569

AMERICAN INSTITUTE OF AERONAUTICS AND ASTRONAUTICS • 1633 BROADWAY • NEW YORK, N.Y. 10019

Aerodynamics of Two-Dimensional Blade-Vortex Interaction

G. R. Srinivasan*

JAI Associates, Inc., Mountain View, California
andW. J. McCroskey† and J. D. Baeder‡
U.S. Army Aeroflightdynamics Directorate—AFSCOM
NASA Ames Research Center, Moffett Field, California

Unsteady interaction of a helicopter rotor blade with a passing vortex is numerically calculated using the two-dimensional, thin-layer Navier-Stokes equations and a prescribed vortex approach at subsonic and transonic flow conditions. The results are compared with the recent experimental data of Caradonna et al. for a two-bladed rotor in forward flight. The comparisons show that, for the subcritical flow case, the unsteady lag effects on the basic rotor blade are absent and the three-dimensional effects appear to be negligible. The numerical results are in good agreement with the experimental data. At the supercritical flow condition, however, the flowfield is dominated by the presence of the shock waves, with strong indications of unsteady time lags in the shock-wave motions and strengths and of important three-dimensional effects, even in the absence of the vortex interaction. Hence, for this case, the two-dimensional calculations fail to predict the basic rotor flowfield. The presence of strong three-dimensional influence in the supercritical flow data is demonstrated through transonic small disturbance calculations, whereas similar calculations for the subcritical flow condition showed almost no three-dimensional influence. Finally, the details of the experimental vortex structure were found to be important in matching the numerical results with the experimental data.

Nomenclature

A, B, C, C_1, C_2	= coefficients, see Eq. (1)	ϵ	= unknown flowfield vector
D, E		ψ	= Euler solution of vortex in an uniform freestream
\hat{A}, \hat{B}	= Jacobian matrix	R	= radius of rotor blade
a	= vortex core radius	R_c	= Reynolds number
a_s	= freestream sound speed	r	= radial distance from the vortex center
C	= characteristic length scale (chord) of the rotor blade	r_s	= reference station on the rotor blade
C_L	= lift coefficient	r_0	= initial vortex position ($= 0$ in y)
C_M	= quarter chord pitching moment coefficient	r_0	= ϵ (Eq. 1)
C_p	= pressure coefficient	r_0	= ϵ (vortex flow center)
C_x	= chord of the vortex generating wing	r_0	= ϵ (time)
\hat{E}, \hat{F}	= flux vector	U	= intravortex velocity component
E, F	= total energy per unit volume	U_x	= forward velocity of vortex in tunnel wind
\hat{F}	= flux vector	U_y	= velocity components in physical plane
I	= identity matrix	U_z	= velocity components induced by the vortex
J	= transformation Jacobian	V	= tangential velocity of vortex
M	= Jacobian matrix of a shear stress flux vector	x	= instantaneous vortex position
M_L	= local Mach number	x	= physical plane coordinate
M_R	= blade reference Mach number ($= 1.0$)	x_s	= airfoil surface ($= 0$ at $x_s = 0$)
M_{R_s}	= blade tip Mach number	α	= angle of attack
M_∞	= freestream Mach number	β	= vortex strength
P	= static pressure	β_0	= dimensionless strength (Euler)
Q	= velocity induced by the vortex	β_0	$= 1/M_\infty$ or $= M_\infty/1$
		γ	= ratio of specific heat
		δ	= airfoil thickness ratio
		ϵ	= inverse of blade aspect ratio ($= 1/A$)
		ϵ	= explicit and implicit smoothing coefficients, respectively
		θ	= angle between the vortex velocity vector and x -axis
		θ	= angle between vortex axis and rotor blade chord
		λ	= advance ratio ($= V_\infty/U_\infty$)
		λ	= local advance ratio ($= V_\infty/U_\infty$)
		λ	= metric of transformation
		λ	= transformed plane coordinate

Presented at Paper 86-176 at the AIAA 19th Aerospace Sciences Meeting, Plasmadynamics and Laser Conference, 1986, New Orleans, La., Aug. 4-6, 1986; received Sept. 1, 1986; revised Sept. 22, 1986. This paper is asserted to be the author's original work and is offered to AIAA for possible publication. It has not been submitted to another organization. Copyright claimed here by the author. All rights reserved. AIAA member rights are reserved by the copyright owner.

*Senior Research Scientist, Member AIAA.

†Senior Staff Scientist, Associate Fellow AIAA.

‡Research Scientist, Member AIAA.

ρ	= density
Φ	= disturbance potential
ψ	= azimuth angle (Fig. 2)
Ω	= angular velocity of the rotor blade

Introduction

ONE important problem of helicopter aerodynamics that has been the subject of many recent experimental¹⁻⁴ and theoretical⁵⁻¹¹ studies is the mechanism of blade-vortex interaction. This interaction mechanism is a primary source of impulsive noise generation. The transonic speeds of today's helicopter blade tips add to the complexity of the problem. The blade tips, which trail the strong and concentrated tip vortices in such a flowfield, trace out prolate cycloidal paths in space, and, in the process, encounter a variety of blade-vortex interactions. These interactions induce unsteady blade loading and aerodynamic noise, with compressibility playing an important role in the problem.

The generic problem of the blade-vortex interaction can be viewed, in general, as unsteady and three-dimensional; however, in one limit, when the intersection angle of the vortex with the blade (Λ) is very small or zero, the interaction can be approximated to be two-dimensional but unsteady, (see Fig. 1) Most of the recent numerical studies⁵⁻¹¹ that have addressed this problem have been solved in this limit. Transonic small-disturbance equations,^{5,6} full-potential equations,^{7,8} Euler equations,^{9,10} and thin-layer Navier-Stokes equations¹¹ all have been solved for the problem of a convecting vortex passing and interacting with the flowfield of a stationary airfoil in a uniform freestream.

Some of the preceding methods place limitations on the intensity of the interaction in terms of vortex strength, vortex location with respect to the airfoil, and on the freestream Mach number; nevertheless, they all seem to give similar

results. For flows dominated by the strong viscous interaction and shock-wave/boundary-layer interaction, the natural choice of the equation set that describes such a flow completely would be the Navier-Stokes equations. Present-day numerical algorithms for this set of equations are still very expensive in terms of computing time, although much progress has been made toward reducing the time required. However, the memory of the available computers is adequate to address these types of problems in the two-dimensional limit. This is particularly true with the present prescribed-vortex, or perturbation, method which has been demonstrated to resolve important flow features in a blade-vortex interaction problem in both subsonic and transonic flows, even in a very sparse finite difference mesh.¹²

A problem more practical and numerically more complicated than the one mentioned previously is that of a rotating blade of a helicopter rotor encountering a vortex generated upstream. Such an experiment was done recently in a wind tunnel at the U.S. Army Aeromechanics Laboratory (presently called Aeroflightdynamics Directorate, U.S. Army Aviation Research and Technology Activity—AVSCOM) at NASA Ames Research Center.¹³ A schematic of the experiment is shown in Fig. 2. A vortex generated at the tip of a straight NACA-0015 wing interacts with the flowfield of a rotating, two-bladed helicopter rotor blade under subsonic and transonic flow conditions. For such a rotating blade, unlike the stationary airfoils considered in previous studies,⁵⁻¹¹ the unsteady time-lag effects that are present even in the absence of the interacting vortex are very important.¹⁴ The effect of this unsteady time lag is to delay the process of flow adjustment corresponding to the appropriate azimuthal blade position. This has a profound influence on the unsteady blade loads at transonic conditions. In addition, the results may also be influenced by the three-dimensional tip effects, if the chordwise reference station considered is closer to the blade tip. Another very important ingredient of the vortex interaction study is the detailed knowledge of the structure of the interacting vortex. Although an analytical representation of the vortex is often used, the point to bear in mind is that such a representation should have an accurate core structure embedded in it.

In the present investigation, it was found that the rotor-blade reference station of Ref. 1 (section AA in Fig. 2) that undergoes parallel blade-vortex interaction is inboard of the blade tip region. If the tip influence is neglected at this station, the flow can be approximated as two-dimensional, but unsteady. One important difference of this problem from the earlier formulation⁵⁻¹¹ is that the blade is rotating now. After implementing this important feature, along with the necessary changes in the boundary conditions, unsteady, two-dimensional, thin-layer Navier-Stokes equations in strong conservation-law form are solved for the interaction flowfield of the rotating blade using an approximately factored, implicit, finite difference numerical algorithm written in delta form.¹⁵⁻¹⁷ An analytical representation of the measured vortex structure was used in the computations.

Although the initial finite difference grids were generated by an algebraic method,¹⁴ an adaptive-grid procedure¹⁸⁻²⁰ was used throughout to resolve the important flow features, including shock waves, vortex, shock-induced separation of the boundary layers, if any, and the vortex structure itself.

In this paper, the governing equations and numerical formulations are discussed, and the numerical results and comparisons with experimental data are presented.

Governing Equations and Solution Procedure

The interaction flowfield is solved by the prescribed-vortex, or perturbation, method.¹² The essence of the method is that each of the dependent flow variables is split into a prescribed part, which is simply the vortical disturbance, and a remaining part, which is obtained from the solution of the governing

Fig. 1 Schematic of parallel blade-vortex interaction, in the limit of $\Lambda = 0$, and definition of coordinate system.

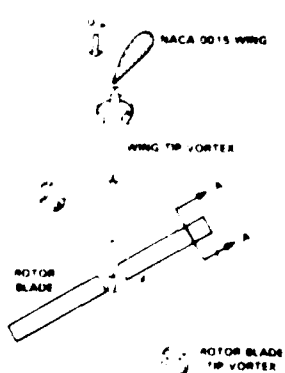


Fig. 2 Schematic of experimental model rotor tests of Ref. 1.

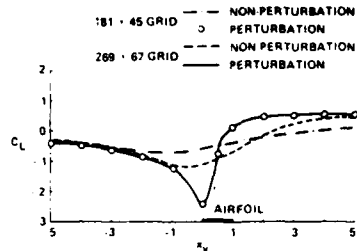


Fig. 3 Effectiveness of the prescribed-vortex method compared with the nonperturbation method. Euler results for airfoil-vortex interaction: NACA 64A006 airfoil, $M_\infty = 0.85$, $\alpha = 0$ deg, $\hat{t} = 0.2$, $a_0 = 0.05$, and $y_0 = y_o = -0.26$.

equation set. Even though the governing equations are nonlinear and independent solutions are not superposable, the dependent variables can still be decomposed as

$$\mathbf{q} = \mathbf{q}_0 + (\mathbf{q} - \mathbf{q}_0)$$

where

$$\mathbf{q} = \begin{bmatrix} \rho \\ \rho u \\ \rho v \\ e \end{bmatrix} \quad \text{and} \quad \mathbf{q}_0 = \begin{bmatrix} \rho \\ \rho u \\ \rho v \\ e \end{bmatrix}_v \quad (1)$$

Here \mathbf{q} is the unknown flowfield vector, and the vector \mathbf{q}_0 represents the solution of Euler equations for the vortical disturbance convecting in a uniform freestream. Previous studies^{7,9} have demonstrated that the perturbation method can, in fact, resolve the flows with concentrated vortices well, even with a coarser grid when compared to a nonperturbation method.¹⁸ For example, a representative plot of the variation of lift coefficient as a function of the vortex position is reproduced from Ref. 8 in Fig. 3. This calculation was done using Euler equations for the case of a convecting vortex encountering a nonlifting, stationary NACA-64A006 airfoil in transonic flow, and using the same grid topology with both perturbation and nonperturbation (or conventional) methods. This figure clearly demonstrates that with the conventional method the accuracy of the solution increases with the fineness of the finite difference mesh, whereas the perturbation method produces a much better solution even in a coarser mesh.

The governing partial differential equations are the unsteady, thin-layer Navier-Stokes equations.¹⁹ The equations are written in nondimensional, strong conservation-law form for a perfect gas using the generalized independent coordinate system of

$$\xi = \xi(x, y, t), \quad \eta = \eta(x, y, t), \quad \tau = \tau(t) \quad (2)$$

and in the perturbation form^{7,9} as

$$\partial_t(\hat{\mathbf{q}} - \hat{\mathbf{q}}_0) + \partial_\xi(\hat{\mathbf{E}} - \hat{\mathbf{E}}_0) + \partial_\eta(\hat{\mathbf{F}} - \hat{\mathbf{F}}_0) = Re^{-1} \partial_\eta \hat{\mathbf{S}} \quad (3)$$

where $(\hat{\cdot})$ denotes quantities scaled by the Jacobian, e.g.,

$$\hat{\mathbf{q}} = J^{-1} \mathbf{q}; \quad \hat{\mathbf{q}}_0 = J^{-1} \mathbf{q}_0 \quad (4)$$

and

$$J = \xi, \eta, -\xi, \eta, = 1 / (x_\xi, y_\eta - x_\eta, y_\xi)$$

is the transformation Jacobian. The flux vectors $\hat{\mathbf{E}}$, $\hat{\mathbf{E}}_0$, $\hat{\mathbf{F}}$, $\hat{\mathbf{F}}_0$, and $\hat{\mathbf{S}}$ are described in detail in Refs. 7-9. The viscous flux vector $\hat{\mathbf{S}}$ is written in the context of a thin-layer model¹⁹ and, hence, is valid for high-Reynolds-number turbulent flows. The

turbulent eddy viscosity is computed using a two-layer, algebraic eddy-viscosity model.²⁰

The generalized coordinate system of ξ , η , τ allows the boundary surfaces in the physical plane to be mapped onto rectangular surfaces in the computational plane. This feature simplifies the procedure of grid-point clustering in the flow regions that experience rapid change in the flowfield gradients.

The primitive variables that make up the governing equations, Eq. (3), are density ρ , the two mass fluxes ρu and ρv in the two coordinate directions x and y (where x is the streamwise direction and y is normal to it), and the total energy per unit volume, e . All length scales are normalized by the chord of the rotor blade at the reference station, and the dependent variables ρ , p , e , u , and v by ρ_∞ , p_∞ , $\rho_\infty a_\infty^2$, and a_∞ , respectively.

The pressure, density, and velocity components are related to the energy per unit volume by the equation of state, which is written for a perfect gas as

$$e = \frac{p}{\gamma - 1} + \rho \left(\frac{u^2 + v^2}{2} \right) \quad (5)$$

This equation of state, along with the mass and momentum equations given by Eq. (3), completes the equation set to be solved.

In the present formulation, the difference between the problems of the stationary and moving blades shows up in the metric terms involving time derivatives, namely, ξ_t and η_t . Following the formulation given by Isom²¹ and Caradonna and Isom²² for unsteady flow over helicopter rotor blades, the effective local Mach number at the reference station can be written as

$$M_r = M_\infty (1 + \mu' \sin \Omega t) \quad (6)$$

where M_∞ is the rotational Mach number, μ' the local advance ratio, and Ω the angular velocity of the rotating blade. This formulation enables the flowfield solution of a rotating blade with an oncoming freestream to be solved in the two-dimensional limit as a blade moving with an x velocity of $M_\infty a_\infty \mu' \sin \Omega t$ in a flow of Mach number M_∞ . Note that both ξ_t and η_t are nonzero for this case, whereas, for a stationary blade with a fixed grid, both ξ_t and η_t are zero.

The boundary conditions are applied explicitly. Since the grid extends 20 chord lengths in all directions from the surface of the blade, freestream conditions are specified at the outer boundary and simple extrapolation is used for ρ , ρu , and ρv at the outflow boundary. For supersonic flow, the total energy e is also extrapolated; but for subsonic flow, the pressure is held constant at the freestream value, and e is obtained from Eq. (5). To ensure continuity across the wake cut, the flow variables are linearly extrapolated to obtain the values along the cut.

Along the body surface $\eta(x, y, t) = 0$, the no-slip condition for viscous flow without suction or injection is given by setting U and $V = 0$. The pressure along the body surface is obtained by solving the normal momentum equation, and the density at the surface is obtained by extrapolation from the grid interior. The total energy e is calculated from the known pressure and density at the surface. The boundary conditions are of low order and, hence, require that the grid be clustered and normal at the body surface.

The interacting vortex is initialized at an upstream location of the airfoil, typically at or near the upstream grid boundary as in Ref. 9. The vortex flow vector $\hat{\mathbf{q}}_0$ is determined as follows. The cylindrical velocity is analytically prescribed either by a Lamb-like distribution or by fitting a smooth curve through the experimental data, if available. For this vortex convecting in a uniform freestream, the induced pressure and density fields are determined numerically by solving the radial momentum equation in conjunction with the energy equation for constant enthalpy flow. With the velocity, density, and

pressure fields known, the total energy e_v is determined from the energy equation.

Surface conforming grids are needed to simplify the application of the body-boundary condition procedure. In this study, an adaptive gridding procedure of Nakahashi and Deiwer^{15,16} is used to resolve flow features and to improve the accuracy of the numerical method. Briefly, the method uses tension and torsion spring analogies. The tension spring, which connects the adjacent grid points to each other, controls grid spacings so that clustering is obtained in regions containing shock waves and shear layers. On the other hand, the torsion spring, which is attached to each grid node, controls inclinations (angles) of coordinate lines and prevents excessive grid skewness. The mesh can be made nearly orthogonal at the surface. A marching procedure is used that results in a simple tridiagonal system of equations at each coordinate line to determine the grid-point distribution. Multidirectional grid adaptation is achieved by successive application in each direction. For the compressible flowfields considered in this study, the density gradient was found to be the best choice to drive the adaption in the x direction; the Mach number gradient was the best choice of driver in the normal direction. In actual practice, for a given baseline grid, the preceding procedure will modify the grid at specified intervals to resolve the flow satisfactorily. In the present study, the grid was adapted at every two marching steps interval. This increased the computational time by approximately 50%. The baseline grid used was a surface-conforming C-grid generated by an algebraic method of Pulliam et al.¹⁴ and had 221 points around the airfoil and 67 points in the normal direction. The grid boundary was chosen to be at 20 chords in all directions.

An implicit, spatially factored numerical algorithm with Euler-implicit time differencing¹³ is used to solve the perturbation form of Eq. (3). This algorithm is written in delta form as

$$\begin{aligned} & (I + h \delta_\xi \hat{A}^n - \epsilon_I J^{-1} \nabla_\xi \Delta_\xi J) \\ & \times (I + h \delta_\eta \hat{B}^n + h \delta_\eta \hat{M}^n - \epsilon_I J^{-1} \nabla_\eta \Delta_\eta J) (\Delta \hat{q}^n - \Delta \hat{q}_0^n) \\ & = -\Delta_I [\delta_\xi (\hat{E}^n - \hat{E}_0^n) + \delta_\eta (\hat{F}^n - \hat{F}_0^n) - Re^{-1} \delta_\eta \hat{S}^n] \\ & - \epsilon_E J^{-1} [(\nabla_\xi \Delta_\xi)^2 + (\nabla_\eta \Delta_\eta)^2] J (\hat{q}^n - \hat{q}_0^n] \quad (7) \end{aligned}$$

where \hat{A} , \hat{B} , and \hat{M} are the Jacobian matrices detailed in Ref. 19, I the identity matrix, δ_ξ and δ_η the spatial central difference operators, and Δ and ∇ the forward and backward difference operators, respectively. For convenience, $\Delta_\xi = 1 - \Delta_\eta$ is assumed. The time index is denoted by h , and $\hat{q}^n = \hat{q}^n(n \Delta t)$, $\Delta \hat{q}^n = \hat{q}^{n+1} - \hat{q}^n$, and ϵ_I and ϵ_E are the implicit and explicit smoothing coefficients, respectively. Second-order implicit and fourth-order explicit numerical dissipation terms are added to the numerical scheme to improve the nonlinear stability limits posed by the fine mesh.²³ Even so, the nondimensional time steps generally were restricted by the stability constraints to the order of 0.05 deg of the azimuthal travel of the blade motion or 0.005455 of the chord travel.

The numerical scheme is first-order accurate in time and second-order accurate in space. Further, in writing Eq. (7), it is assumed that $\hat{A}_0 \approx \hat{A}$ and $\hat{B}_0 \approx \hat{B}$, where $\hat{A}_0 = \partial \hat{E}_0 / \partial \hat{q}_0$ and $\hat{B}_0 = \partial \hat{F}_0 / \partial \hat{q}_0$.

Central differencing is used throughout the solution domain, except in regions of supersonic flow before shock waves, where upwind differencing is used. The transformation metrics are not known analytically and are computed numerically by central differencing (second order) at the interior points and by three-point, one-sided differencing at the boundaries.

Results for a Stationary Rotor Airfoil

In this section, numerical results are presented for a moving vortex encountering a fixed rotor blade under transonic condi-

tions. All calculations are done for an NACA-0012 airfoil in a uniform freestream of $M_\infty = 0.8$ at $\alpha = 0$ deg, and assuming a turbulent boundary layer. As mentioned previously, an adaptive gridding procedure is used in all of the results presented here.

A Lamb-like vortex with a finite viscous core ($a_0 = 0.05$) and a cylindrical velocity distribution given by^{7,9}

$$\frac{v_\theta(r)}{a_\infty} = \frac{\tilde{\Gamma}}{2\pi r} M_\infty \left(1 - e^{-r^2/a_0^2}\right) \quad (8)$$

was chosen to interact with the flowfield of a stationary, nonlifting rotor airfoil in a uniform freestream of Mach number M_∞ . The strength of the vortex and its location with respect to the airfoil were chosen to be $\tilde{\Gamma} = 0.2$ and $y_c = -0.26$, respectively. The interaction flowfield was computed in the same manner as outlined in earlier studies.^{7,9} Figure 4 shows plots of instantaneous surface-pressure distributions, the local grid arrangement, and the Mach number contours for different x locations of vortex positions as the vortex passes by the airfoil. The passing vortex induces on the airfoil a continually changing effective angle of attack. Because of the sense of rotation, it induces a downwash initially when it is upstream of the leading edge, changing to upwash as it passes behind the airfoil. This induces a continuous change in the blade-loading pattern. It should be noted here that the initial lift on the blade is zero and that any lift generated during the interaction is induced solely by the vortex. As observed previously,^{7,9} the maximum influence of the vortex on the airfoil flowfield seems to occur when the vortex is within one chord of the airfoil.

Previous calculations done for the same airfoil under identical conditions²⁴ used a fixed-grid topology, with 221×67 grid points; in that study, the shocks were not well resolved. In the present case, the adaptive-grid topology, shown in Fig. 4, also uses 221×67 grid points, but is clearly able to resolve all aspects of the flow. Since the grid is adapted in both the x and y directions, it clearly resolves shock waves, the interacting vortex, and the viscous layer at the body surface. Large-scale vortex and shock-induced boundary-layer separation was not observed, although the formation of a small separation bubble and sufficient thickening of the boundary layer were seen behind the shock wave for conditions when the vortex influence was maximum.

As the vortex passes the airfoil, it encounters the shock wave sitting on the surface. The vortex actually splits the shock wave into a triple shock wave, as is clearly seen from the local grid structure and Mach contours of Fig. 4 for a vortex position past the airfoil midchord. This feature was confirmed by making an independent Euler calculation of the same flow, by using a fixed-grid topology, and by heavily clustering the grid in the region of interest. This apparent unsteady effect seems to fade away as the vortex passes several chords downstream of the airfoil trailing edge. Figure 5 shows a plot of instantaneous lift and pitching-moment coefficients as a function of the x -vortex position during the interaction process. The lift coefficient is initially negative (because of the sense of rotation of the vortex), reaches a negative maximum for a vortex position slightly upstream of the leading edge of the airfoil, increases to a near-zero value at $x_c \approx 7\%$, and stays near that value for the rest of the interaction period. Pitching-moment changes are maximum when the vortex is within 1C of the airfoil.

Results for a Rotating Blade

In this section, computational results are presented corresponding to two experimental conditions of Caradonna et al.¹ One condition each of subcritical and supercritical flows with and without vortex encounter will be discussed. The corresponding tip Mach number of the two cases is 0.6 and 0.8, respectively, with an advance ratio of $\mu = 0.2$ for both.

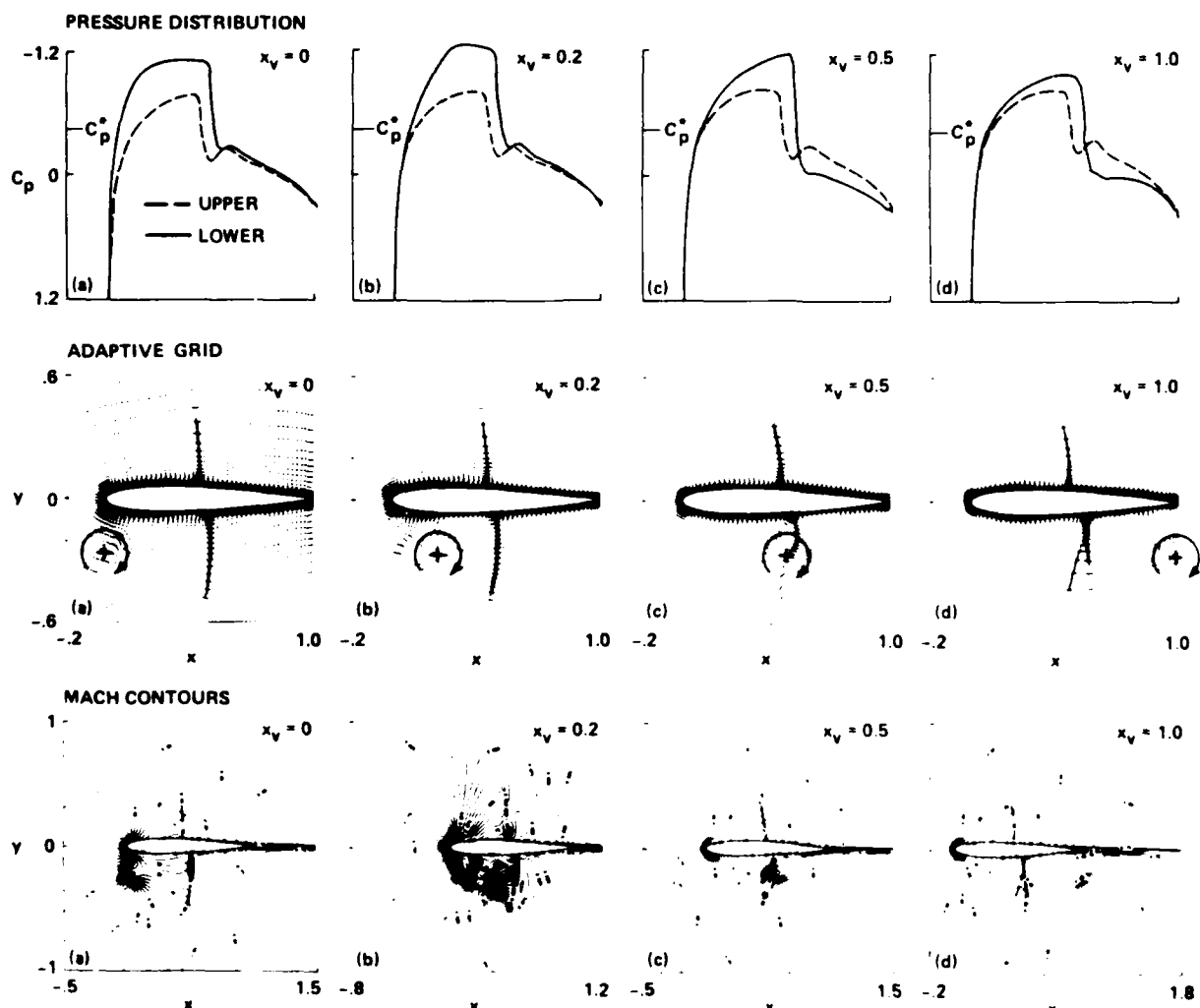


Fig. 4 Instantaneous surface-pressure distributions, adaptive grid, and Mach contours during airfoil-vortex interaction with a convecting vortex: NACA 0012 airfoil, $M_\infty = 0.8$, $\alpha = 0$ deg, $Re = 6 \times 10^6$, $\hat{r} = 0.2$, $y_0 = y_v = -0.26$. The instantaneous position of the vortex during the interaction is shown on the adaptive grid.

The schematic of the experimental arrangement is shown in Fig. 2. The experiments were performed in a wind tunnel where an NACA-0015 wing generated a tip vortex upstream of a two-bladed, model helicopter rotor. The interacting vortex, of core radius 25 mm, passed the reference rotor spanwise station at $r_0 = 0.893$ and at a distance of $y_v = -0.4C$. The chord of the rotor blade was 152.4 mm, and the diameter of the rotor was 2.134 m.

Structure of the Experimental Vortex

Comparison of the numerical results and the experimental data will be meaningful only if the correct structure of the experimental vortex is considered. The strength of the experimental vortex quoted in Ref. 1 is $\hat{r} = 0.31$ with a core radius of $a_0/C = 0.1667$. Use of these data in Eq. (8) yielded peak velocities some 40% greater than those measured by Takahashi and McAlister²⁵ and Orloff and Grant²⁶ for the identical wing under comparable flow conditions, although it had the inviscid vortex, $(1/r)$, behavior well outside the viscous core.

Since the details of the blade-vortex interaction are sensitive to the vortex structure and its peak-induced velocities, the following alternative fit to the experimental data, given by

$$\frac{v_0}{\Omega r_0} = \mu' \frac{\ell_1}{\ell_\infty} = \frac{0.8\hat{r}}{2\pi r} \left(\frac{r^2}{r^2 + a_0^2} \right) \quad (9)$$

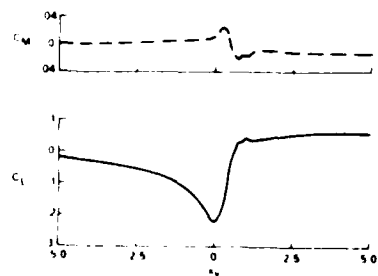


Fig. 5 Lift and pitching-moment variations with instantaneous vortex position for the conditions of Fig. 4.

was used in the numerical calculations. The factor 0.8 was chosen to allow the best match of peak velocity in the available experimental data over the range of angles of attack. Figure 6 shows the resultant agreement with the data^{25,26} at the wing incidence used by Caradonna et al.¹ as well as the inviscid behavior.

Subcritical Case

This condition corresponds to $M_\infty = 0.6$ and $\mu = 0.2$. For the reference station at 89.3% of the rotor blade radius, these conditions translate to $M_\infty = 0.536$ and $\mu' = 0.223$.

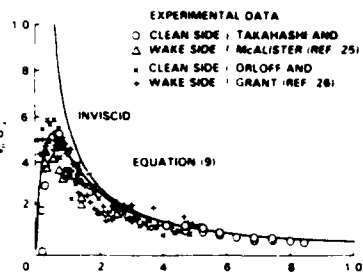


Fig. 6 Tangential velocity distribution of the tip vortex generated by an NACA 0015 wing.

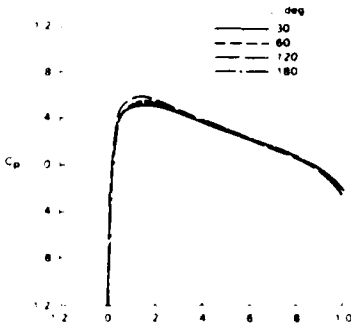


Fig. 7 Instantaneous pressure distributions at the reference blade station for the rotor-alone case: $M_t = 0.6$, $\mu = 0.2$, $r_b = 0.893$.

Results for Rotor Alone

First, consider a nonlifting rotor in forward flight in the absence of vortex interaction. The objective of such an exercise is to determine the importance of three-dimensional, unsteady time-lag effects as the rotor sweeps in azimuth, say, from 0 to 180 deg. As the blade rotates from 0 to 180 deg, its local Mach number increases in the first quadrant, reaching a maximum at the $\psi = 90$ deg position; it again decreases to the average value at $\psi = 180$ deg. In going through this change in local Mach number, if the flow on the rotor at $\psi = 90 + \Delta\psi$ is nearly the same as that at $\psi = 90 - \Delta\psi$, then the rotating blade behaves as if it were quasisteady and quasi-two-dimensional. If, on the other hand, the two flows are different, then the associated three-dimensional or time-lag effects will be expected to have an influence on the vortex-blade interaction flowfield that develops in the vicinity of the $\psi = 180$ deg position.

Figure 7 shows instantaneous surface-pressure results at several azimuth positions of the blade. For this flow, the initial local Mach number for $\psi = 0$ deg is 0.536 and increases to a maximum (based on the local advance ratio) at $\psi = 90$ deg and again decreases to 0.536 at $\psi = 180$ deg. Examination of these pressure distributions indicates that for this subcritical flow condition the unsteady time-lag effects are negligible.

Vortex Encounter with a Rotating Blade

To compute the vortex interaction flowfield, as before, the vortex was initialized at the $\psi = 0$ position of the rotor blade (the corresponding $x_r = -19.638$) as in Refs. 7-9. It then convects with the flow at the effective "freestream velocity," which is $M_t a_\infty (1 + \mu' \sin \psi)$ in this case. Typical instantaneous surface-pressure distributions are shown in Fig. 8 corresponding to several vortex positions as the vortex convects past the rotor blade. Since the rotor is nonlifting, the lift is initially zero, and, as the vortex approaches the blade, it induces a downwash and hence a negative lift. This continuously increases and reverses in sign, becoming positive lift as the

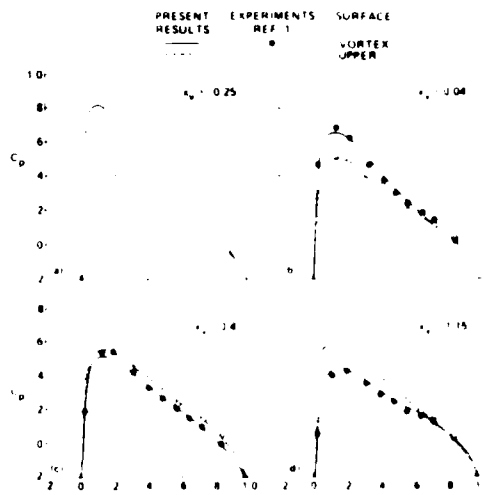


Fig. 8 Instantaneous surface-pressure distributions for the case of blade-vortex interaction. $M_t = 0.6$, $\mu = 0.2$, $r_b = 0.893$, $T = 0.31$, $\psi = -0.4$.

vortex passes the airfoil. Shown in this figure are data from experiments of Caradonna et al.¹ The comparison of numerical results and experimental data shows good agreement, both qualitatively and quantitatively, although the peak pressures on the side of the blade opposite the vortex seem to be underpredicted. It should be pointed out here that, in the experiments, the rotor model had pressure taps on one surface only. To get the pressure distribution on both of the surfaces, the model was simply inverted, and a second, almost identical, experiment was run. Nevertheless, it is gratifying to see such good agreement with experiments. Thus far, three-dimensional effects have been neglected, whose influence at this flow condition appears minimal.

Supercritical Case

This condition corresponds to a tip Mach number of 0.8, with an advance ratio of 0.2, and the blade reference station $r_b = 0.893$, as before. This translates to a reference Mach number of 0.714 and a local advance ratio μ' of 0.223.

Results for Rotor Alone

We first present results for the rotor-alone case (i.e., in the absence of vortex interaction). Figure 9 shows plots of instantaneous surface-pressure distributions at four rotor blade azimuthal positions. As before, the initial lift on the rotor blade (at $\psi = 0$ deg) is zero and the flow is subcritical; as the blade rotates, its local effective Mach number increases, reaching a maximum at $\psi = 90$ deg and decreasing in the second quadrant. As seen in these pressure-distribution plots, the shock wave that develops as the blade rotates gets stronger and moves toward the trailing edge of the airfoil. Even though the effective local Mach number reaches a maximum for $\psi = 90$ deg, the shock wave continues to get stronger and move toward the trailing edge in the second quadrant before it begins moving upstream toward the leading edge of the blade. This unsteady time lag in the growth and decay of the shock wave persists even when the rotor blade has passed the 180 deg azimuthal position into the third quadrant.

Comparison of experimental data² with numerical results in Fig. 9 shows relatively good agreement concerning the pressure levels for all blade azimuthal positions up to $\psi = 150$ deg, but the location of the shock wave is too far aft in the second quadrant. In the experiments, the shock wave seems to have collapsed between the azimuth positions of $\psi = 150$ and 180 deg. But the numerical results show the

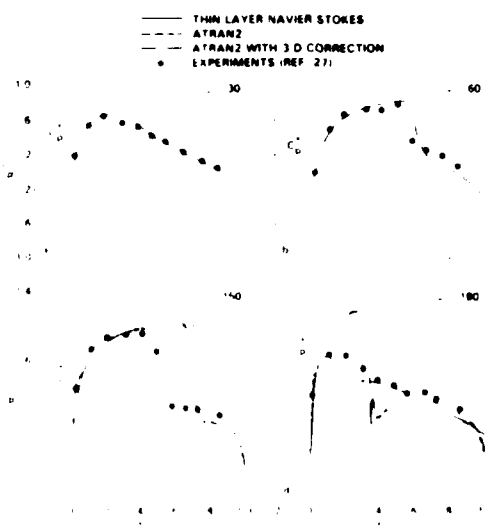


Fig. 9 Instantaneous surface-pressure distributions for the rotor-alone case: $M_f = 0.8$, $\mu = 0.2$, $r_g = 0.893$

persistence of a strong shock wave even at the $\psi = 180$ deg azimuth position, see Fig. 9d. This strongly suggests the presence of possible three-dimensional effects in addition to the unsteady shock-wave lag effects. An attempt is made to examine this aspect using transonic small-disturbance equations as described in the following paragraph.

Some ad hoc insights into possible three-dimensional influences can be obtained from the transonic small-disturbance equation for a thin, high-aspect ratio rotating blade

$$4\Phi_z + B\Phi_z = \frac{1}{c} [(C\Phi_z + C'\Phi_z^2) + \Phi_z + D\Phi_z + E\Phi_z] \quad (10)$$

where Φ_z is the perturbation potential, z the spanwise coordinate, A , B , C , and C' are constants that depend on M_f and the airfoil thickness ratio, and

$$D = -2M_f\mu\cos\Omega t(z + \mu\sin\Omega t)/\delta^2$$

$$E = c'/\delta^2$$

Equation (10) reveals by inspection that three-dimensional effects influence the solution through the two terms, $D\Phi_z$ and $E\Phi_z$. The coefficient E is independent of Mach number, and the term $E\Phi_z$ is undoubtedly important in the immediate vicinity of the tip of the rotor blade. On the other hand, the coefficient D is clearly dependent upon Mach number, as well as the blade aspect ratio, the azimuth of the rotor blade, the spanwise station along the blade, and the local advance ratio, $\mu' = U_\infty/\Omega r_g$, of the rotor. Therefore, it seems likely that this term might play the dominant three-dimensional role inboard of the tip, especially under transonic conditions.

A qualitative estimate of the influence of this cross-flow term was deduced from two-dimensional calculations in which $D\Phi_z$ was added as an inhomogeneous "source" term to the basic small-disturbance code ATRAN2.²⁰ Namely, separation of variables, $\Phi(z, y, z, t) = F(z)\phi(y, t)$, was assumed. $D\Phi_z$ was evaluated by assigning arbitrary constants to the ratio F'/F at a fixed $z = r_g$, and $d\phi/dz$ was evaluated at the previous time step. It was found that negative values of F'/F tended to strengthen the shock wave for $0 \text{ deg} < \psi < 90 \text{ deg}$ and to weaken it for $90 \text{ deg} < \psi < 180 \text{ deg}$, while positive values of F'/F had the opposite effect. For example, Figs. 9c and 9d show that the small-disturbance calculations with

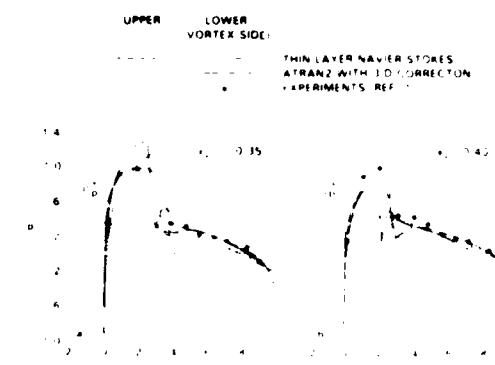


Fig. 10 Instantaneous surface-pressure distributions for the case of blade-vortex interaction: $M_f = 0.8$, $\mu = 0.2$, $\tilde{t} = 0.31$, and $\tilde{t}_v = -0.4$.

$F'(z)$, $F(z) \approx -0.2$ approximately mimic the experimentally observed weakening of the shock wave for $150 \text{ deg} < \psi < 180 \text{ deg}$, whereas both two-dimensional results are seriously in error, by overpredicting the effects, for this supercritical case. On the other hand, results for the subcritical case depicted in Fig. 7 were found to be completely insensitive to similar corrections due to this source term (estimates of $D\Phi_z$).

It must be emphasized that this reasoning is only intended to illuminate the relative importance of cross-flow effects in sub- and supercritical flows, and not to predict such effects accurately. However, this leads us to suggest that the supercritical cases of Ref. 1, with or without the vortex, are neither quasi-two-dimensional nor quasisteady. This stands in sharp contrast to the previous subcritical cases, Figs. 7 and 8, where the two-dimensional calculations are in excellent agreement with the model rotor data, and for which the only significant unsteady effects are solely a result of the airfoil-vortex interaction.

Vortex Interaction with Rotor Blade Section

A previous attempt¹ to compute the blade-vortex interaction flowfield for the supercritical case without considering the unsteady time-lag effects produced unsatisfactory results in terms of the agreement with experiments. Such a disagreement is not surprising in view of the strong time lags and three-dimensional effects present at this supercritical condition. Figure 10 shows the results of the present calculations, including the unsteady time-lag effects, for two z locations of the vortex position during the interaction. The numerical results are calculated from both the two-dimensional, thin-layer Navier-Stokes and the modified (with the three-dimensional correction factor) transonic small-disturbance codes and are compared with the experimental data of Caradonna et al.¹ As before, the two-dimensional results overpredict the interaction effects. However, the ad-hoc three-dimensional correction to the transonic small-disturbance code (ATRAN2) seems to produce results that are in good qualitative agreement with the experiment. It should be noted that, even for this supercritical flow condition, the flow on the experimental rotor blade is subcritical (with zero lift) in the absence of the vortex interaction for the azimuth position $\psi = 180$ deg (see Fig. 9). The interacting vortex modifies the flowfield to be supercritical with strong shock waves as the interaction effects peak. As the vortex passes downstream of the blade, these supercritical conditions progressively change to subcritical conditions. Also, due to the vortex interaction, the blade develops lift which is initially negative (because of the sense of rotation of the vortex), becoming positive as the vortex passes downstream of the blade. In view of the strong viscous interaction nature of this problem, it is not surprising to see less than perfect agreement of the experiments with the approximate calculations of the transonic small-disturbance code, as shown in

Fig. 10. The purpose was only to demonstrate the existence of three-dimensional influence at the supercritical flow conditions.

Concluding Remarks

This paper presents a computational procedure to calculate the interaction flowfield of a passing vortex with a helicopter rotor blade in forward flight and numerical results for subsonic and transonic flow conditions. The interaction of the vortex considered here is one of the limiting cases of a more complex interaction typically encountered on a helicopter rotor blade and corresponds to the parallel blade-vortex interaction experimental conditions of Caradonna et al.¹ In this limit, the interaction flowfield had been previously thought to be two-dimensional and unsteady.

The present numerical scheme involves the solution of unsteady, two-dimensional, thin-layer Navier-Stokes equations implicitly using the perturbation or the prescribed-vortex approach presented in Refs. 7-9. The computational procedure is very general and accepts any arbitrary size and shape of the interacting vortex, although the structure of the vortex is assumed to remain unaltered by the interaction. From comparison of the present numerical results with the experiments, it was found that the details of the vortex structure were important.

Two test cases, a subsonic and a transonic condition corresponding to the experimental data, were chosen for the calculations. The respective blade tip Mach numbers were 0.6 and 0.8, and the blade advance ratio was 0.2. A comparison of the numerical results for these two conditions showed a very distinct difference in the flowfields, even in the absence of the interacting vortex.

The results show that, for the subcritical case, the unsteady time-lag effects are negligible for the rotating blade in the absence of the vortex, and that the unsteady flowfield with the vortex interaction is in very good qualitative and quantitative agreement with experiments. However, the supercritical case is totally dominated by strong (transonic) shock waves, the consequence of which is the presence of strong unsteady time-lag effects even in the absence of the vortex interaction. In addition, there are strong indications of the influence of three-dimensional effects. The experimental data for the rotor-alone case show the collapse of the shock wave between azimuth positions of 150 and 180 deg. The numerical results, on the other hand, show the persistence of a strong shock wave even at the 180 deg azimuth position and, thus, over-predict the experimental data.

Finally, the possibility of three-dimensional effects in the experiment, which was originally thought to be quasi-two-dimensional, was examined further using transonic small-disturbance equations with an ad-hoc three-dimensional correction. The results suggest that the three-dimensional and unsteady time-lag effects are of comparable importance, that both are negligible in purely subcritical flow, and that neither can be ignored when shock waves are present.

Acknowledgments

The research of the first author was partially supported by the U.S. Army Research Office Contract DAAG29-85-C-0002. The authors would like to express their sincere thanks to Dr. J. L. Steger for some stimulating discussions.

References

- Caradonna, F. X., Laub, G. H., and Tung, C., "An Experimental Investigation of the Parallel Blade-Vortex Interaction," Paper 4, Tenth European Rotorcraft Forum, The Hague, the Netherlands, Aug. 1984.
- McAlister, K. W. and Tung, C., "Airfoil Interaction with an Impinging Vortex," NASA TP 2273, 1984.
- Meier, G. E. A. and Timm, R., "Unsteady Vortex Airfoil Interaction," Paper 16, AGARD CP 186, AGARD Symposium on Unsteady Aerodynamics: Fundamentals and Applications to Aircraft Dynamics, May 1985.
- Padakannaya, R., "Experimental Study of Rotor Unsteady Airloads due to Blade-Vortex Interaction," NASA CR-1907, 1971.
- Caradonna, F. X., Tung, C., and Desoppe, A., "Finite-Difference Modeling of Rotor Flows Including Wake Effects," *Journal of the American Helicopter Society*, Vol. 29, No. 2, April 1984, pp. 26-33.
- George, A. R. and Chang, S. B., "Noise due to Transonic Blade-Vortex Interactions," Paper A-83-39-50-D000, 39th Annual National Forum of the American Helicopter Society, May 1983.
- Srinivasan, G. R., McCroskey, W. J., and Kutler, P., "Numerical Simulation of the Interaction of a Vortex with a Stationary Airfoil in Transonic Flow," AIAA Paper 84-0254, Jan. 1984.
- McCroskey, W. J. and Srinivasan, G. R., "Transonic Interaction of Unsteady Vortical Flows," Paper 5-1, Third Symposium of Numerical and Physical Aspects of Aerodynamic Flows, Long Beach, CA, Jan. 1985; also, NASA TM-86658, 1984.
- Srinivasan, G. R., "Computations of Two-Dimensional Airfoil-Vortex Interactions," NASA CR-3885, 1985.
- Wu, J. C., Sankar, N. L., and Hsu, T. M., "Unsteady Aerodynamics of an Airfoil Encountering a Passing Vortex," AIAA Paper 85-0203, Jan. 1985.
- Jones, H. E., "The Aerodynamic Interaction Between an Airfoil and a Vortex in Transonic Flow," Paper presented at the Workshop on Blade-Vortex Interactions (unpublished), NASA Ames Research Center, Moffett Field, CA, Oct. 1984.
- Caradonna, F. X. and Philippe, J. J., "The Flow over a Helicopter Blade Tip in the Transonic Regime," *Vertica*, Vol. 2, No. 1, 1978, pp. 43-60.
- Beam, R. M. and Warming, R. F., "An Implicit Finite-Difference Algorithm for Hyperbolic Systems in Conservation-Law Form," *Journal of Computational Physics*, Vol. 22, Sept. 1976, pp. 87-109.
- Pulham, T. H., Jespersen, D. C., and Childs, R. E., "An Enhanced Version of an Implicit Code for the Euler Equations," AIAA Paper 81-0344, 1983.
- Nakahashi, K. and Deiwert, G. S., "A Practical Adaptive-Grid Method for Complex Fluid-Flow Problems," *Lecture Notes in Physics*, Vol. 218, Springer-Verlag, 1984, pp. 422-426; also, NASA TM-85989, 1984.
- Nakahashi, K. and Deiwert, G. S., "A Self-Adaptive-Grid Method with Application to Airfoil Flow," AIAA Paper 85-1525-CP, 1985.
- Buning, P. G. and Steger, J. L., "Solution of the Two-Dimensional Euler Equations with Generalized Coordinate Transformation Using Flux Vector Splitting," AIAA Paper 82-0971, June 1982.
- Srinivasan, G. R., Chu, W. J., and Steger, J. L., "Computation of Simple Three-Dimensional Wing-Vortex Interaction in Transonic Flow," AIAA Paper 81-1206, June 1981.
- Steger, J. L., "Implicit Finite-Difference Simulation of Flow about Arbitrary Two-Dimensional Geometries," *AIAA Journal*, Vol. 16, July 1978, pp. 679-686.
- Baldwin, B. S. and Lomax, H., "Thin Layer Approximation and Algebraic Model for Separated Turbulent Flows," AIAA Paper 78-257, Jan. 1978.
- Isom, M. P., "Unsteady Subsonic and Transonic Potential Flow over Helicopter Rotor Blades," NASA CR 2463, 1974.
- Caradonna, F. X. and Isom, M. P., "Numerical Calculation of Unsteady Transonic Potential Flow over Helicopter Rotor Blades," *AIAA Journal*, Vol. 14, April 1976, pp. 482-488.
- Pulham, T. H. and Steger, J. L., "On Implicit Finite-Difference Simulations of Three-Dimensional Flow," *AIAA Journal*, Vol. 18, Feb. 1980, pp. 159-167.
- Srinivasan, G. R. and McCroskey, W. J., "Computations of Blade-Vortex Interaction by Different Methods," Paper presented at the Workshop on Blade-Vortex Interactions (unpublished), NASA Ames Research Center, Moffett Field, CA, Oct. 1984.
- Takahashi, R. K. and McAlister, K. W., "Preliminary Measurements of a Wing-Tip Vortex Using Laser Velocimetry," U.S. Army Aeroflightdynamics Directorate, NASA Ames Research Center, Moffett Field, CA, 1985, personal communication.
- Orloff, K. L. and Grant, G. R., "The Application of Laser Doppler Velocimetry to Trailing Vortex Definition and Alleviation," NASA TM X-62,243, 1973.
- Tung, C., U.S. Army Aeroflightdynamics Directorate, NASA Ames Research Center, Moffett Field, CA, 1985, personal communication.
- McCroskey, W. J. and Goorjian, P. M., "Interactions of Airfoils with Gusts and Concentrated Vortices in Unsteady Transonic Flow," AIAA Paper 83-1691, July 1983.

END

DATE

FILMED

5-88

DTIC